Propagation over rounded hills

**THE BRITISH BROADCASTING CORPORATION
ENGINEERING DIVISION**

RESEARCH DEPARTMENT

PROPAGATION OVER ROUNDED HILLS
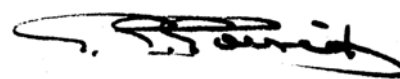
Research Department Report No. RA-21

UDC 621.391.812.8 1968/30

K. Hacking, B.Sc.

Head of Research and Development

(RA-91)

PROPAGATION OVER ROUNDED HILLS

PROPAGATION OVER ROUNDED HILLS

SUMMARY

Several features of the diffraction of electromagnetic waves by large obstacles are examined both theoretically and by optical experiments using a laser source and idealized models. The underlying purpose of the work was to establish and verify, where possible, working methods for estimating the field strength in the shadows of rounded hills. The emphasis throughout is for the special conditions which arise in u.h.f. broadcasting, where ordinary terrain has a near-dielectric behaviour and its surface becomes effectively rough. Hill curvature in the direction of propagation is shown to be an important factor. An attempt is made to deal with hill crests whose surfaces are randomly rough and with those of irregular shape.

List of Principal Symbols

E	= relative field strength
v,p,q	= Fresnel parameters, $v = (2D/\lambda)^{1/2}\,\theta$
θ	= angle of diffraction
R	= radius of curvature
λ	= wavelength
r	= excess-loss parameter $= (\pi R/\lambda)^{1/3}\theta$
d_0	= standard distance $= (R^2\lambda/\pi)^{1/3}$
d_1	= distance of transmitter to edge in single-edge problems
d_2	= distance of receiver to edge in single-edge problems
d	= distance between transmitter and receiver $(d_1 + d_2 = d)$
D	= effective distance $= (d_1 d_2/d)$

a,b,c	= spacing distances in double-edge problems $(a + b + c = d)$
α	= measure of effective separation of two edges = arctan $(bd/ac)^{1/2}$
ϵ_r	= complex relative permittivity
ρ_V, ρ_H	= Fresnel reflection coefficients for vertically polarized and horizontally polarized radiation respectively
γ	= grazing angle (complementary angle of incidence)
h	= height of edge above line joining transmitter and receiver
x	= height variable
ϕ	= acute angle between the common tangent of a double crest and the transmitter horizon.

1. INTRODUCTION

The planning of a network of u.h.f. television transmitting stations is a formidable undertaking, since hundreds of sites must be selected and the radiation characteristics must be specified for each of them. In order to reduce the amount of field-strength measurement entailed in this process there is a growing interest in methods of field-strength prediction by computer. In predicting field strength within the service area the principal problem is to estimate the effect of diffraction over hills and other obstacles into regions which are out of sight of the transmitting aerial. This problem cannot be solved exactly, and prediction is in practice a process of theoretical approximation modified as necessary by empirical corrections.

The work described in this report was intended to establish, and verify where possible, working methods for estimating the field strength in the shadow of hills of comparatively simple shape. The report is largely concerned with the relationship between the profile of the diffracting edge in the direction of propagation and the rate of the transition from light to dark.

The separations of source, obstacle and receiver are considered here to be very large compared with the wavelength. The obstacles are also large, and are generally supposed isolated from the source and receiver. These conditions correspond to many situations arising in ultra-high-frequency (u.h.f.) broadcasting, where a hill or ridge directly obscures the transmitter and the ground waves reflected from the intervening terrain can be neglected.

A rather surprising fact, which can be demonstrated both theoretically and experimentally, is that the distant e.m. field at points close to the geometrical shadow boundary is hardly affected by the curvature of the diffracting crest, i.e. whether it is sharp or blunt. Within this boundary region of the shadow, which is defined more precisely below, every hill or ridge behaves like a knife-edge (opaque half-plane) for which the Fresnel diffraction pattern is well known. As we explore deeper into the shadow field, however, the roundedness and surface properties of the diffracting crest have increasingly significant effects on the e.m. field and the treatment of rounded obstacles as knife-edges can lead to large errors in field-strength prediction.

2. BACKGROUND TO THE INVESTIGATION

2.1. Classical Approach to Diffraction

The classical approach to diffraction problems is to apply Huygens' principle to the aperture above the obstacle. For example, diffraction at a thin screen or knife-edge, as shown in Fig. 1(a), is treated by supposing that each elementary area in the plane (PQ) above the screen behaves as a secondary source of radiation with an amplitude and relative phase determined by that of the incident wave in the absence of the screen. The resultant field at a point R is obtained by a vector summation of all the fields due to the hypothetical sources in the aperture. This method is not rigorous because it assumes that the field in the aperture is not perturbed from its free-space value by the presence of the screen. However, for the knife-edge problem, the assumption holds good for distances above the edge greater than a few wavelengths. For small angles of diffraction ($<10°$ say) the contribution to the distant field from a strip immediately above the edge a few wavelengths high is small, so that the classical solution is a very good approximation. Note, too, that the solution is independent of the polarization of the incident wave.

Suppose that this approach is applied now to a smooth, gently curved edge as shown in Fig. 1(b). Again consider the plane aperture (PQ) above the top of the crest. It will be seen that specular reflections from the crest-surface to the left of P will perturb the free-space field for many wavelengths above P. Similarly, the field at R due to a Huygens' source above P will be influenced by the addition of a specularly reflected component from the crest-surface to the right of P. Furthermore, if the specularly reflected waves undergo a phase reversal, destructive interference is likely to occur. The amplitude of the field in the perturbed strip above P can then be expected to diminish and, for the same reason, so will the field at R due to

sources in the strip. Consequently, under these conditions, it is clear that a gently curved edge will produce a lower field-strength and cast a sharper shadow than a knife-edge.

The field-reducing effect caused by the specularly reflected components is mitigated if the surface in the region of the crest is made rough, since strength of the reflections will then be impaired. The result will be a return towards the knife-edge field.
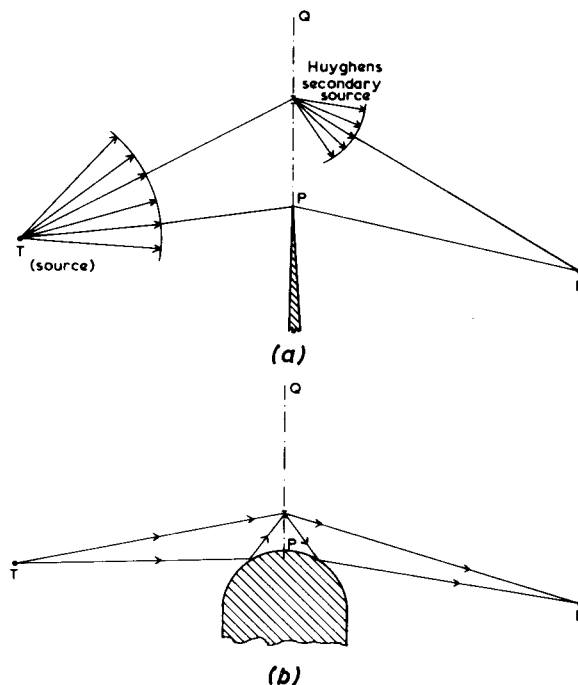
Fig. 1 - Classical approach to diffraction
(a) Sharp edge (knife-edge)   (b) Gently curved edge

2.2. Inadequacy of the Knife-Edge Approximation

There is mounting evidence from u.h.f. propagation measurements that predictions based solely on a knife-edge approximation to rounded-hill profiles generally over-estimate the field-strength in the shadow. Crysdale, et al[1], found, during a study of very-high-frequency (v.h.f.) and u.h.f. propagation over a mountain ridge in Çanada, discrepancies between measured and predicted field-strengths of approximately 5 dB and 15 dB at 173 MHz and 493 MHz respectively; subsequently[2] application of a correction for the mean curvature of the ridge, using the theoretical result given by Rice[3] for diffraction by a parabolic cylinder, largely eliminated the discrepancies.

As further evidence, a comparison of field-strength measurements* obtained during the site

Fig. 2 - Typical ground height-profile encountered in S. Wales

N.B.: This profile has an exaggerated vertical scale and assumes the Earth's radius to be increased by a factor 4/3 to allow for normal atmospheric refraction

testing of u.h.f. relay stations in South Wales with theoretical predictions derived from the ground profiles may be cited. Several ground profiles between the transmitter and a mobile receiver were analysed, of which the one shown in Fig. 2 is typical. The majority of the paths involved diffraction by more than one hill. In Fig. 3, whi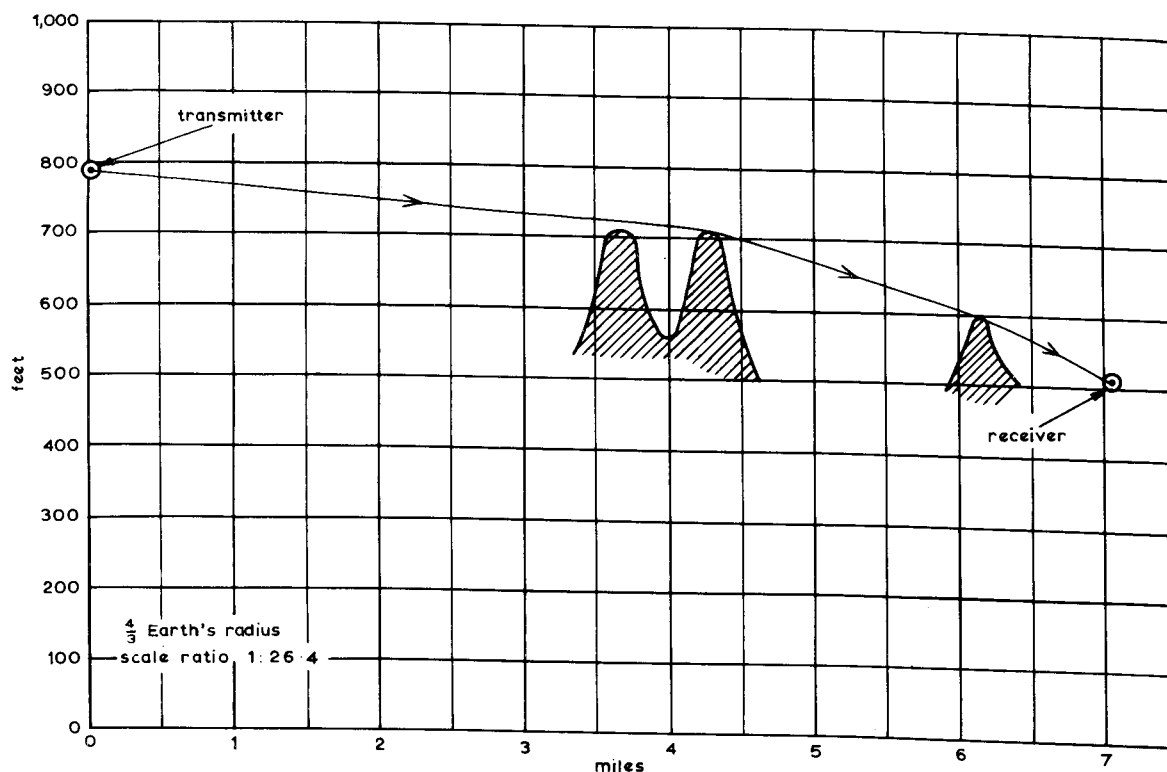ch shows the results of this comparison, the predicted field-strength is plotted against the measured field-strength; each particular path link is indicated by a vertically-disposed pair of plot points. Clearly, if the measured and theoretical results were in perfect agreement, all the points would lie on a straight line through the origin inclined at 45° to the axes. The open-circle data are obtained on the assumption that each diffracting crest along the profile is a perfect knife-edge, and the dashed line drawn on the Figure is the least-squares fit to this set of data assuming the measured values to be correct. The solid-circle data, however, were obtained by estimating the mean curvatures of the diffracting crests and then applying a correction for each based on methods which are discussed later in this report; the full-line curve is the least-squares fit to the solid-circle data.

It will be seen from Fig. 3 that, in the region where the measured field strength is low, the knife-edge assumption tends to overestimate the field strength, and that taking the crest curvatures into account considerably reduces the average error (in

fact, the slope of the least-squares line indicates a slight over-correction for hill curvature). At high field strengths, however, which correspond to paths where the terminals are only just obstructed by hills, it will be noted that equivalent knife-edge methods are adequate.
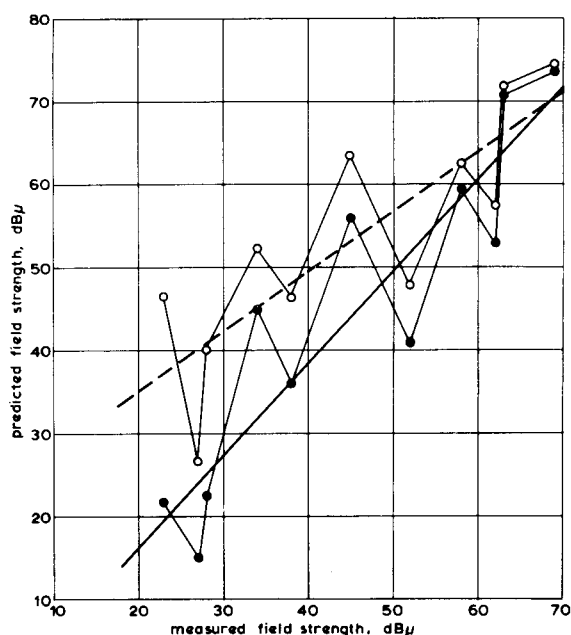

Fig. 3 - Comparison of predicted and measured field strengths for eleven paths in S. Wales

__o__ Predictions based on knife-edge theory

__•__ Predictions based on rounded-hill theory

4

2.3. Rice's Criterion

The well-known classical solution for the field behind a perfect knife-edge, relative to the free-space field*, is given in terms of a complementary Fresnel integral by

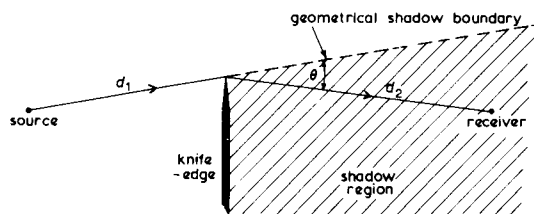$$E(v) = \frac{1-j}{2} \int_v^\infty \exp(j\pi z^2/2)\, dz \qquad (1)$$

Fig. 4 - Notation and geometry for knife-edge diffraction

where (see Fig. 4)

$v = (2D/\lambda)^{1/2}\, \theta$ (Fresnel parameter)

θ = angle of diffraction (positive measured into the shadow)

$D = d_1 d_2/(d_1 + d_2)$

and λ = wavelength

On the geometrical shadow boundary $v = 0$ and $|E(v)| = \frac{1}{2}$, for $v>0$ the relative field diminishes as v increases and, for v large and positive,

$$|E(v)| \simeq (2^{1/2}\pi v)^{-1}.$$

Note also that v varies inversely with $\lambda^{1/2}$.

Now Rice[3] suggests the criterion $(R/\lambda)^{1/3}\theta<\frac{1}{4}$ for the validity of the knife-edge approximation to a hill crest whose mean radius of curvature is R, although the limit $\frac{1}{4}$ is somewhat arbitrary. It can be shown that, in terms of the Fresnel parameter v, this criterion would correspond approximately to $v<1$ for gently curved hills and $v<3$ for the sharper crests encountered in prediction work. At u.h.f. broadcast frequencies (i.e. approximately 500 to 900 MHz) many situations arise where the v parameter lies in the range 3 to 5 and, therefore, significant errors can be expected if a knife-edge approximation is used. At v.h.f. broadcast frequencies, on the other hand, the v parameter rarely exceeds 2 because of the larger wavelength so that neglecting the curvature of the crests is not expected to lead to gross errors in the majority of situations.

* $E(v)$ is a ratio of field strengths. The total diffraction loss for a perfect knife-edge is defined as -20 log₁₀ $|E(v)|$ decibels. Here, and throughout this report, a time factor $\exp(-j\omega t)$ has been suppressed.

2.4. Surface Irregularities

The exact solutions for diffraction by large cylinders and spheres are usually tractable only if it is assumed that the surfaces are perfectly smooth. In u.h.f. (and v.h.f.) broadcasting over populated terrain, however, structures such as buildings, trees etc. have dimensions of many wavelengths and may be scattered in varying densities over the surface, making it effectively rough. It is true that the built-up areas tend to be in the valleys rather than on hill crests but gently curved hills on the outskirts of large towns are often residential areas.

The question arises — can we apply the smooth-surface diffraction solutions, when calculating the field in the shadow of rough hills, with reasonable accuracy? The diffraction experiments at microwave frequencies carried out by Bachyinski[4] indicated that roughening the surface tends to make it behave more like a knife-edge, although the degree of roughness was not stated. One of the major purposes of the experimental investigation described here was to obtain quantitative data about the effects of random-type surface roughness which can be used to guide u.h.f. prediction work.

2.5. Profiles of Varying Curvature

In some instances the profile of the diffracting crest, even if smooth, cannot easily be approximated by a single arc of constant curvature. In this class are crests with flat tops and crests with double-hump profiles for which practical methods of estimating their shadow fields are more obscure. Idealized models of such profiles were investigated experimentally, in order to provide data against which theoretically-derived methods of calculation may be tested.

2.6. Surface Conductivity

U.H.F. propagation measurements[5] show that differences in the shadow field strength due to the orientation of the plane of polarization of the incident wave are not marked. Generally, a vertically-polarized wave is the more easily propagated beyond the horizon, especially at the lower frequencies where the ground behaves like a good conductor. As we approach the u.h.f. bands, however, the complex relative permittivity of ordinary terrain has a progressively smaller imaginary part and it therefore approaches dielectric behaviour. For example, ground of high conductivity, $\sigma \approx 2 \times 10^{-2}$ mhos/m say, has a complex relative permittivity ϵ_r given by

$$\epsilon_r \approx 25 - j(360/f)$$

where f is the frequency in MHz. Thus at u.h.f. ϵ_r is largely real, since the displacement currents predominate.

The Fresnel formulae for the specular reflection coefficient of an e.m. wave at a plane boundary are

$$\rho_V \approx \frac{\sin \gamma - (1/\epsilon_r)^{\frac{1}{2}}}{\sin \gamma + (1/\epsilon_r)^{\frac{1}{2}}} \quad \text{for vertical polarization and}$$

$$\rho_H \approx \frac{\sin \gamma - (\epsilon_r)^{\frac{1}{2}}}{\sin \gamma + (\epsilon_r)^{\frac{1}{2}}} \quad \text{for horizontal polarization,}$$

where $(\pi/2 - \gamma)$ is the angle of incidence. These show that for values of ϵ_r obtaining at u.h.f. there is a small yet considerable range of grazing angles for which $\rho_V \approx \rho_H \approx -1$. Consequently, in diffracting over profiles of shallow curvature, where the angles of incidence in the neighbourhood of the crest are close to grazing, differences in the shadow field strength between the two polarizations will be small.

Some additional polarization differences[5] may arise where diffraction takes place over wooded terrain or shrubland and the wavelength is such that the slim, vertical nature of the tree-trunks can affect, differentially with respect to polarization, the diffuse scattering associated with the reflected waves. This effect is noticeable at v.h.f. and may result in a somewhat lower field strength at the receiving point for vertically-polarized radiation. Again, these differences tend to disappear at u.h.f.

3. THEORETICAL SOLUTIONS

The rigorous solution of the diffracted field has always been a formidable mathematical problem even for simple forms of perfectly-conducting obstacle such as the half-plane, the cylinder and the sphere. A summary of the historical development of the theoretical treatments is given in the introduction to a paper on the subject by Pryce[6], and in another by Wait and Conda[7].

The earlier formal solutions for spheres and cylinders of large radii of curvature involved series which are slowly convergent in the region near the geometrical shadow boundary, thus making numerical evaluation difficult. More recently, Fock[8] used a complex-integral representation of the diffracted field, which led to easier numerical evaluation.

The effects of finite surface conductivity on the diffracted field have received attention in later studies[9,11].

3.1. Numerical Comparison of Several Solutions

The various solutions for the shadow field strength given in four comprehensive theoretical papers[3,9,10,11], differing widely in their respective methods of treatment, are compared numerically here by applying them to a specific diffraction problem.
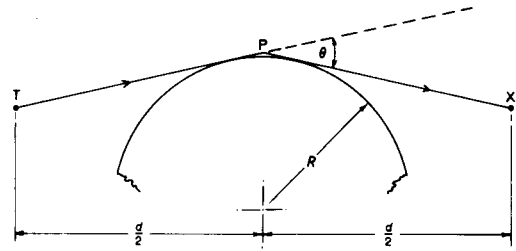

Fig. 5 - Geometry of common arrangement for comparing four theoretical solutions
$$TX = d \qquad D = d/4$$

In the papers by Wait and Conda[9], and Shkarofsky, et al[10], the basic mathematical model was a smooth circular cylinder. In the former paper a rigorous solution of the wave equation was derived, while in the latter a physical-optics approach involving a four-ray construction was used. S.O. Rice[3] considered the diffraction of a plane wave incident on a perfectly-conducting cylinder with a parabolic profile and obtained an exact solution in terms of Airy integrals. The earlier classical solution for diffraction by a sphere was developed (with emphasis on the higher frequencies) into engineering form by Domb and Pryce[11] who considered the diffracted field for a transmitter situated above a smooth spherical earth; numerical calculation was made easier by replacing Hankel functions of order one third by Airy integrals.

For simplicity in the calculations, the symmetrical arrangement of transmitter, obstacle and receiver shown in Fig. 5 was chosen for the numerical comparison. A transmitter, radiating uniformly, is supposed to be situated at the point T, and a receiver situated in the shadow at the point X. Symmetrically placed is a smooth-crested ridge whose effective radius of curvature is R. The diffraction angle, θ, is the acute angle between the tangents to the crest from T and X, which intersect at P. It is assumed that θ is small ($<12°$ say).

Following Domb and Pryce, distances are expressed in terms of a standard distance d_0, where

$$d_0 = \left(\frac{R^2 \lambda}{\pi}\right)^{1/3} \tag{2}$$

A theoretical analysis indicates that when $D \gg d_0$ (Fig. 5) the diffracted field can be expressed as the product of two factors. One of these factors is independent of the radius of curvature of the crest in the direction of propagation and, in fact, is simply the attenuation factor which would be obtained if the obstacle was reduced to a knife-edge placed at P in Fig. 5. Further, the other factor can be expressed as a function of the single (dimensionless) parameter r, where

$$r = \left(\frac{\pi R}{\lambda}\right)^{1/3} \theta \tag{3}$$

Thus a useful normalization is expected if the results are expressed in terms of r, which we might call the 'excess-loss' parameter.

The extent of the mutual agreement between the four theoretical predictions of the shadow field is shown in Figs. 6 and 7, for an incident wave polarized with its electric vector perpendicular to the plane of incidence.

In Fig. 6, the total diffraction loss in decibels is plotted as a function of r, for $(D/d_0) = 25$. It will be seen that numerical agreement is very good, except for the Shkarofsky results for $r > 0.5$: the apparent divergence here is believed to be due to a simple numerical approximation which the authors introduced to simplify the evaluation of the integrals, rather than indicating a fundamental limitation of their method. All the authors are in almost complete agreement at $r = 0$.
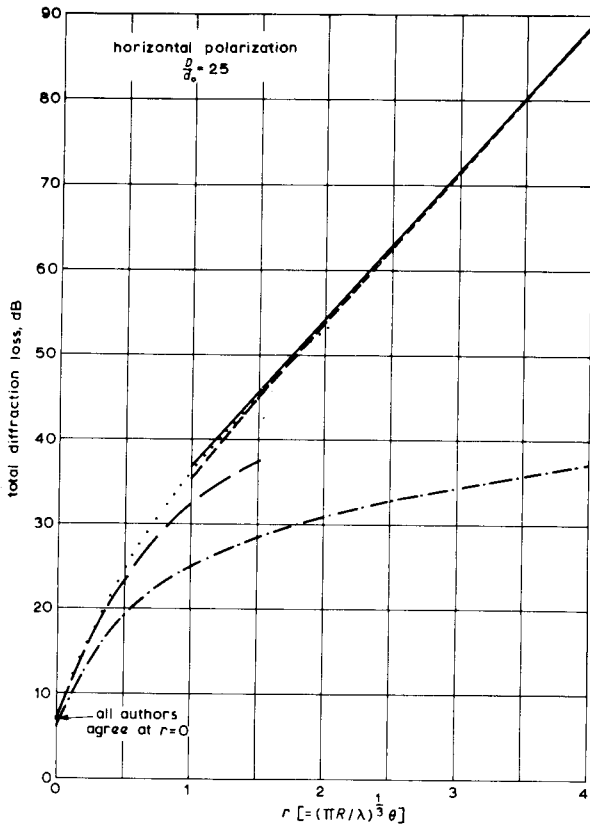

Fig. 6 - Theoretical predictions of diffraction loss

———— Domb and Pryce   — — — — Rice

·······Wait and Conda

— · — Shkarofsky, Neugebauer and Bachynski

- · — - Fresnel (knife-edge solution)

The parameter r is related to the Fresnel limit parameter v (see Section 2.3) by

$$v = \left(\frac{2D}{\pi d_0}\right)^{\frac{1}{2}} r \qquad (4)$$

where $D = d_1 d_2/(d_1 + d_2)$.

(For the symmetrical arrangement shown in Fig. 5 we have $d_1 = d_2 = d/2$, where d is the distance TX, hence $D = d/4$).

We see from Equation (4) that if D/d_0 is assumed constant then v is directly proportional to r. In particular if $D/d_0 = 25$ then $v = 4.0r$ and we can include in Fig. 6 the diffraction loss which would be obtained if the obstacle were replaced by a knife-edge at P (Fig. 5).

In Fig. 7, the diffraction loss in excess of the knife-edge loss is plotted as a function of the distance parameter D/d_0, for several integral values of r. The excess diffraction loss, which is solely due to the finite curvature of the diffracting crest, is seen to be almost independent of the distances of the transmitter or the receiver from the crest, for a given angle of diffraction (r constant). More specifically we might say, from the data in Fig. 7, that this independence holds sufficiently well for most practical purposes if $D/d_0 > 10$.

The essential features of the diffracted field (horizontal polarization) far behind a smooth, rounded hill of shallow curvature are apparent from the above results. On the geometrical shadow boundary the relative field strength is slightly below one-half, approaching more closely one-half as the transmitter and receiver move farther away from the crest. Near the boundary, but moving directly into the shadow, the behaviour is similar to that of a knife-edge although the field strength diminishes at a somewhat faster rate. As we get well into the shadow the field strength varies in an exponential manner in contrast to the hyperbolic variation found for a knife-edge.

3.2. Polarization Effects

It may be shown[9,11] that the effect on the shadow field of the finite permittivity of a smooth cylinder or sphere can be ascertained from the magnitude of the dimensionless parameter Δ, where

$$\Delta_V \approx \left(\frac{\pi R}{\lambda}\right)^{1/3} |\epsilon_r^{-1/2}|$$

for vertical polarization (electric vector in the plane of incidence) and

$$\Delta_H \approx \left(\frac{\pi R}{\lambda}\right)^{1/3} |\epsilon_r^{1/2}|$$

for horizontal polarization. Large increases in the shadow field occur when Δ approaches zero, i.e. when $|\epsilon_r|$ is large for vertical polarization or when R becomes vanishingly small for both polarizations.

As discussed in Section 2.6, for ordinary ground at u.h.f., $|\epsilon_r|$ probably lies in the range 5 — 25.
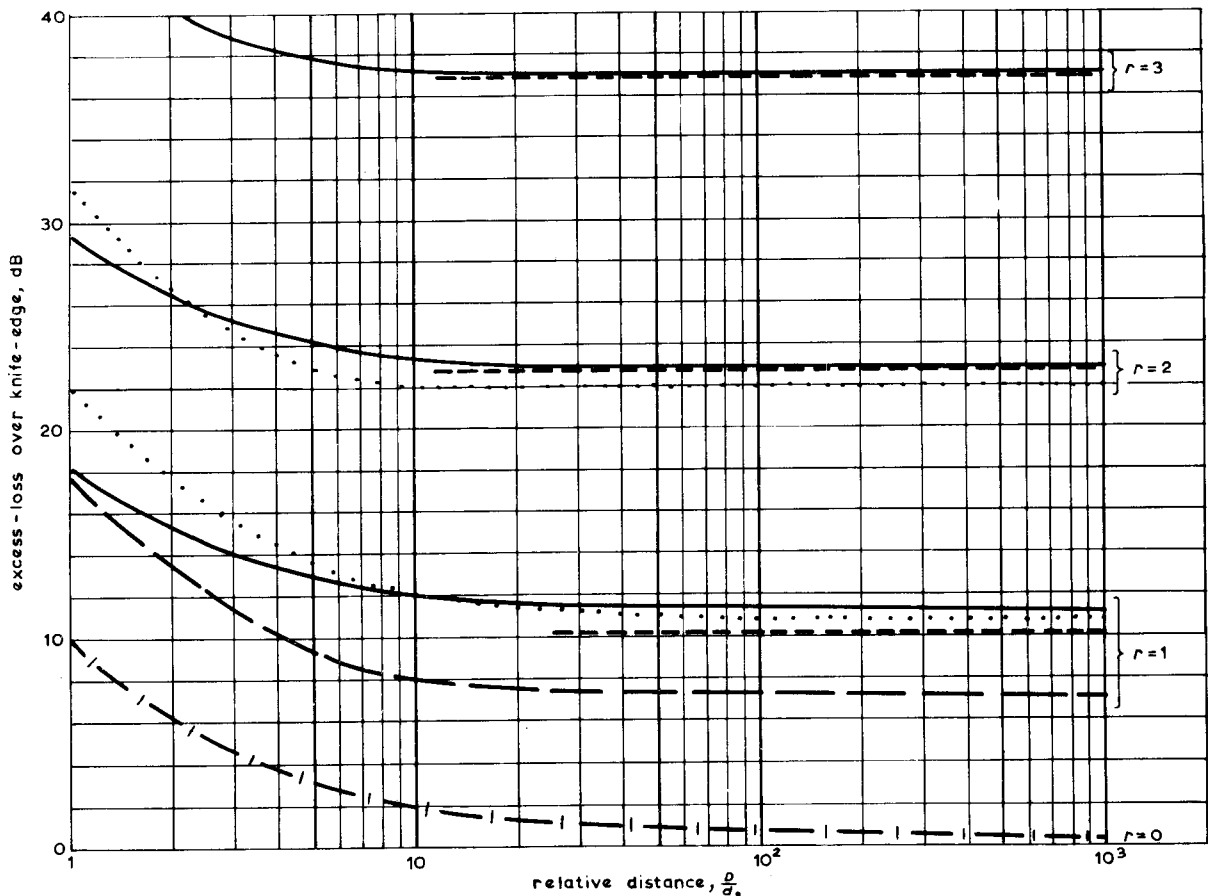
Fig. 7 - Variation of excess-loss with distance

——————— Domb and Pryce ——— — — —Rice .... Wait and Conda

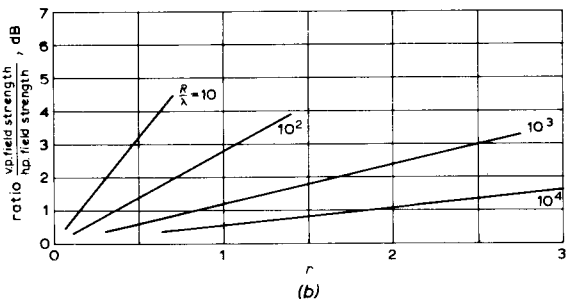——————— ——————Shkarofsky, Neugebauer and Bachynski—— ı—— ı—— All authors

(a)

(b)
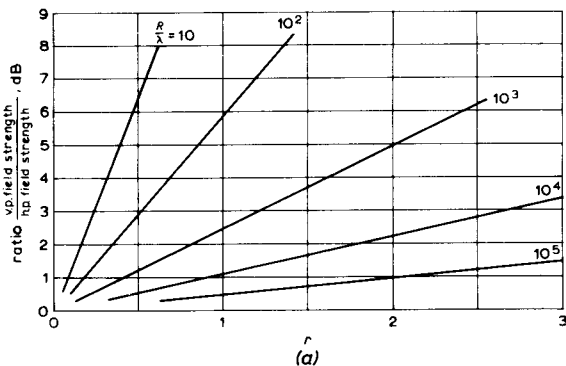
Fig. 8 - Theoretical polarization differences

(a) Smooth ground with $|\epsilon_r| = 25$

(b) Smooth ground with $|\epsilon_r| = 5$

Fig. 8 shows the ratio of the shadow field strength for vertically-polarized radiation to that for horizontal polarization as a function of r, for several values of R/λ: Fig. 8(a) refers to smooth ground with $|\epsilon_r| = 25$ and Fig. 8(b) shows the corresponding situation with $|\epsilon_r| = 5$. These results were calculated using the method proposed by Domb and Pryce[11]. It will be noted that the vertically-polarized field is always the larger, but for the predominant range of parameter values encountered in u.h.f. propagation ($r<2$, $R/\lambda > 10^3$ and $5<|\epsilon_r|<25$) the differences are small.

3.3. Basic Method for U.H.F. Prediction

We see from the general nature of the theoretical solutions that a practical method* of estimating the total diffraction loss, suitable for u.h.f. prediction work, is first to obtain the equivalent knife-edge loss, thereby taking into account the geometry of the situation, and then to add an 'excess-loss' which allows for the finite curvature of the diffracting crest. Thus

Total diffraction loss (dB) =

Fresnel knife-edge loss (dB) + Excess-loss (dB)

* A similar method has been proposed recently by the National Bureau of Standards, see Reference 12.

The Fresnel knife-edge loss is obtained in the usual manner by assuming that the diffracting crest is replaced by a hypothetical knife-edge situated at the intersection of the transmitter and receiver horizons.

If the diffracting crest is effectively smooth and has constant or slowly varying curvature, the excess-loss term is derived from:

(a) A basic (universal) function of the single parameter $r \equiv (\pi R/\lambda)^{1/3}\theta$, as shown in Fig. 9.

(b) A close-distance correction for $D/d_0 < 10$; Fig. 10 shows a set of curves from which the additional loss can be estimated.

(c) A further correction for ground permittivity if the transmission is vertically-polarized and the crest-curvature sharp. This correction may be estimated from the data shown in Fig. 8.

The basic excess-loss function shown in Fig. 9 was derived from Fig. 6. Strictly, this particular excess-loss curve refers to $D/d_0 = 25$ but because of its small dependence on distance (Fig. 7) it holds sufficiently well for practical purposes for $D/d_0 > 10$.
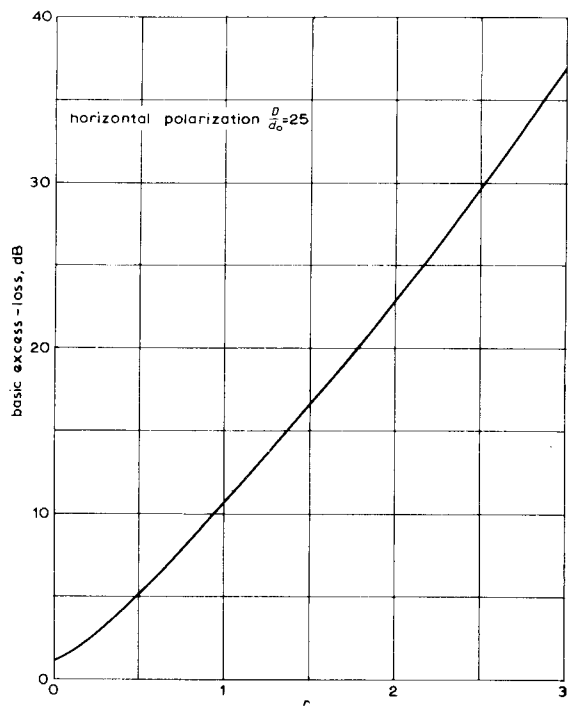

Fig. 9 - Basic excess-loss function

3.4. Multiple Diffraction

An extension of the Fresnel solution for diffraction by a single knife-edge to two knife-edges in tandem has been given by Millington et al[13]; the solution is expressed in terms of Fresnel

surface-integrals, and an investigation of the numerical methods of rapidly evaluating these integrals is presented in a second, companion paper[14].

General solutions to the problem of multiple diffraction by spherical mountains have been obtained by Furutsu[15] in Japan.
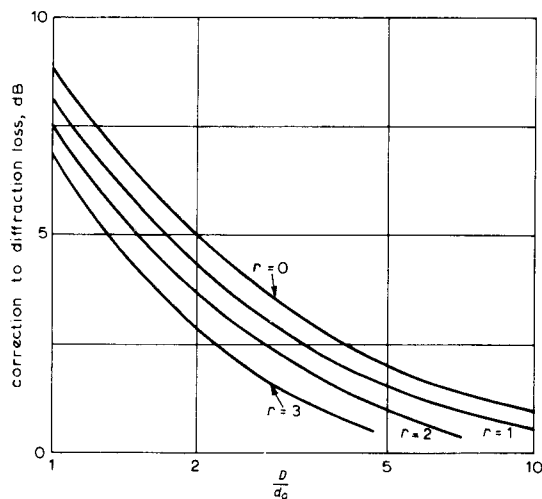

Fig. 10 - Additional loss at close distances $(D/d_0<10)$

An exact evaluation of the field strength in the shadow of two or more rounded hills is somewhat complicated, even if the hill crests can be represented by profiles of constant curvature. There are, however, situations where approximate methods are valid and these being relatively simple to apply are attractive for rapid prediction work. Several known approximate methods for dealing with two knife-edges in tandem were considered by Wilkerson[16], who applied them to a large number of hypothetical configurations of transmitter, receiver and knife-edges. He concluded that no single approximate method was superior for all situations, some methods giving more accurate results for certain configurations.

One approximate method is worth mentioning here because of its validity where successive obstacles (and the receiver) are well into the shadow cast by the preceding one, its easy extension to any number of such obstacles, and its suitability for applying excess-loss corrections for the individual crest curvatures. The method, which originated in Japan[17], can be derived by a direct application of Keller's geometrical theory of diffraction[18,19]. Fig. 11 shows the geometry of a configuration where multiple diffraction occurs with three ridges. A transmitter is situated at T_0 and receiver at X; P_1, P_2 and P_3 are intervening ridges, the inter-separations being d_1, d_2, d_3 and d_4, as shown. The angles of diffraction at each edge are θ_1, θ_2 and θ_3 respectively.
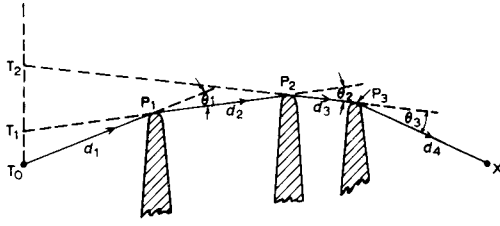
Fig. 11 - Multiple diffraction: construction for the method described in Section 3.4

The relative field strength at P_2, which is in the shadow cast by P_1, is first calculated. If the diffracting edges are initially assumed to have infinite curvature the relative field at P_2 will be $|E(v_1)|$ (see Section 2.3), where the Fresnel parameter v_1 refers to the path $T_0P_1P_2$. This is then multiplied by the relative field which would be obtained at P_3 if P_1 were removed and the transmitter moved to the position T_1, which is a point above T_0 on the line through P_1P_2. This is $|E(v_2)|$ where v_2 refers to the path $T_1P_2P_3$. Finally a third factor $|E(v_3)|$ is obtained which is the relative field at X assuming P_1 and P_2 absent and the transmitter moved to T_2 on the line through P_2P_3. The required relative field strength at X, E_x say, is then given by:

$$E_x \approx |E(v_1)| \times |E(v_2)| \times |E(v_3)| \qquad (5)$$

where

$$v_1 = \left[\frac{2d_1d_2}{\lambda(d_1 + d_2)} \right]^{\frac{1}{2}} \theta_1$$

$$v_2 = \left[\frac{2d_3(d_1 + d_2)}{\lambda(d_1 + d_2 + d_3)} \right]^{\frac{1}{2}} \theta_2$$

and

$$v_3 = \left[\frac{2d_4(d_1 + d_2 + d_3)}{\lambda(d_1 + d_2 + d_3 + d_4)} \right]^{\frac{1}{2}} \theta_3$$

The method is valid if all the v-values are reasonably large (>1.5, say) and when this occurs the method is reciprocal, i.e. the same result is obtained if the transmitter and receiver are supposed interchanged. Significant errors may accrue and failure of reciprocity may occur, however, if one or more of the v-values are close to zero or negative, so that judicious application of the method is necessary.

The finite curvatures of the crests can be taken into account by calculating the excess-loss due to finite curvature for each of the single-obstacle paths $T_0P_1P_2$, $T_1P_2P_3$ and T_2P_3X using the methods given in Section 3.3.

The physical basis of the above method, and of the somewhat similar Epstein-Peterson method[20], is that to an observer well into the shadow cast by

an edge there appears to be a small radiation source actually located on the edge itself. This effect is strikingly demonstrated by illuminating the edge of a razor blade with a spatially coherent beam of light from a laser, and looking at the edge from a position deep in the shadow. The apparent source on the edge is, of course, a virtual one which the eye infers from the way in which the phase varies over the pupil.

3.5. Diffraction by a Thick Slab

In some real-terrain situations the profile of the diffracting crest may exhibit a pronounced flat-top, and the validity of representing such a profile by an equivalent arc of constant curvature, in order to estimate the diffracted field strength, is doubtful. Some indication of the behaviour of this kind of crest-profile can be obtained from the diffracted field behind a thick slab, which is but an extreme form of the flat-top profile.
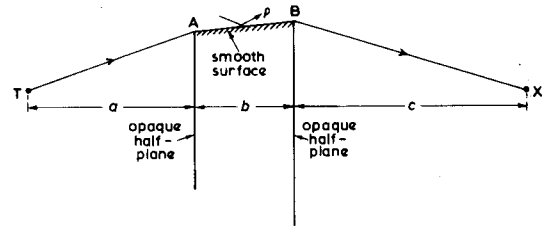
Fig. 12 - Thick-slab representation

It is shown in the Appendix, that a solution for the smooth, thick slab can be obtained in terms of Millington's[13] solution for a double knife-edge, i.e. in terms of Fresnel surface-integrals. We suppose (Fig. 12) that a thick slab is formed by joining two half-planes (in tandem) with a flat surface whose complex Fresnel reflection coefficient* is p. At a given point in the shadow region the relative field strength is the sum of two components, E_1 and E_2 say. The component E_1 is the relative field obtained in the absence of the joining surface and is given by the Fresnel surface-integral (following Millington but with a slight change of notation)

$$E_1 = \frac{-j}{2} \int_S \exp(j\pi z^2/2) \, dS \qquad (6)$$

where z is the polar distance of a point in the (infinite) plane of integration. Fig. 13(a) shows a typical sectorial region of integration S (shaded) which Millington defines by the three parameters p, q and α**. The axes u and w, as well as the

---

* Strictly p is a function of angle of incidence (see Section 2.6) but here we assume it to be constant or only slowly varying over the dominant range of grazing angles.

** The parameters p and q are, in fact, the Fresnel parameters for the first and second edges respectively (i.e. equivalent to v in Equation (1)), while α is a measure of the effective separation of the edges.

parameters p, q and α, are defined in the Appendix (Equations 14, 15 and 17).

The second component E_2 is due to the presence of the joining surface and can also be described by a similar surface integral. Thus

$$E_2 = \frac{-j}{2}\rho \, \exp(j2\pi K) \int_{S'} \exp(j\pi z^2/2) \, dS' \qquad (7)$$
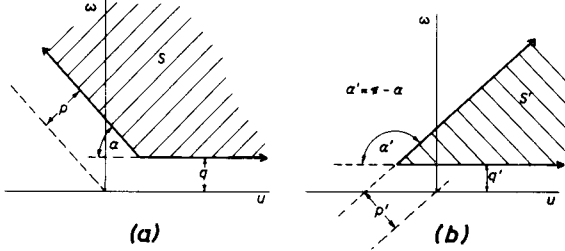

(a) *(b)*

Fig. 13 - Regions of integration, S and S'

(a) 1st component E_1 (direct component)

(b) 2nd component E_2 (reflected component)

where S' is a different region of integration (Fig. 13(b)) defined by the parameters p', q' and α', which can be expressed in terms of p, q and α defining S (again see Appendix). The most important relation is that $\alpha' = \pi - \alpha$, so that if S is large, S' is small and vice-versa. The factor $\exp(j2\pi K)$ in Equation (7) signifies a constant phase shift with respect to the E_1 component; K is a function of p, q and α (see Appendix). It should be noted (Fig. 12) that the parameter $\alpha = \tan^{-1}(bd/ac)^{1/2}$, which might be described in the present context as the obstacle-width coefficient, depends only on the inter-separations of the transmitter, receiver and edges (AB) of the slab.

The total relative field is:

$$E_1 + E_2 = \frac{-j}{2}[I(p,q,\alpha) + \rho \, \exp(j2\pi K)I(p',q',\alpha')] \qquad (8)$$

where $I(p,q,\alpha) = \int_S \exp(j\pi z^2/2) \, dS$. (see Fig. 13(a))

and $I(p',q',\alpha') = \int_{S'} \exp(j\pi z^2/2) \, dS$. (see Fig. 13(b)).

Some special cases are of interest:

(a) $p = q = 0$

This is the situation where the transmitter, receiver and flat top all lie in the same plane. The areas of integration now become true sectors and by simple proportionality we find that $I(p,q,\alpha) = j(\pi - \alpha)/\pi$ and $I(p',q',\alpha') = j\alpha/\pi$. Further, since $K = 0$ we obtain for $\rho = -1$ (horizontal polarization)

$$|E_1 + E_2| = \frac{1}{2}\left(1 - \frac{2\alpha}{\pi}\right) \qquad (9)$$

for the flat top, compared with $\frac{1}{2}(1 - \alpha/\pi)$ for the double knife-edge and simply $\frac{1}{2}$ for a single knife-edge.

If the thick slab is perfectly conducting and the radiation vertically polarized we have $\rho = +1$ and then $E_1 + E_2 = \frac{1}{2}$ so that in this case the flat top behaves as a single knife-edge.

(b) $p = q\cos\alpha$, or $q = p\cos\alpha$

This is the situation where either the transmitter or the receiver lies in the same plane as the flat top. From the parameter relations given in the Appendix we find $q' = q$, $p' = -p$ and $K = 0$.

For horizontal polarization ($\rho = -1$) the relative field strength is, from Equation (8)

$$E_1 + E_2 = \frac{-j}{2}[I(p,q,\alpha) - I(-p,q,\pi-\alpha)] \qquad (10)$$

In general, no simple expression exists for the quantity in the square brackets on the r.h.s. of Equation (10). If α is not too small ($>30°$ say) and the receiver is well into the shadow it can be shown that Equation (10) reduces to

$$|E_1 + E_2| \approx \frac{\cot \alpha}{\pi^2 q^2} \qquad (11)$$

Since $\cot\alpha$ is defined by $(ac/bd)^{1/2}$ we see that for $b \ll d$ (Fig. 12) the field strength well into the shadow is approximately proportional to $b^{-1/2}$, i.e. varies inversely with the square root of the width of the slab.

It is of interest also to compare Equation (11) with the deep-shadow result for a single knife-edge (placed at B, Fig. 12) which is $(2^{1/2}/2\pi q)$. Thus the excess diffraction loss of a flat-top obstacle over that of a knife-edge, when the transmitter is in the same plane as the flat top, is ($\alpha > 30°$, $q > 3$)

$$\text{Excess-loss} \approx 20 \, \log_{10}(2^{-1/2}\pi q \, \tan\alpha), \text{ decibels.} \quad (12)$$

It is concluded that diffracting crests with pronounced flat-top profiles will cast sharp shadows, except when the surface is highly conducting* and the incident radiation vertically polarized. In this event, if the transmitter and/or receiver lies in the plane of the flat top the shadow-field behaviour is similar to that of a single knife-edge.

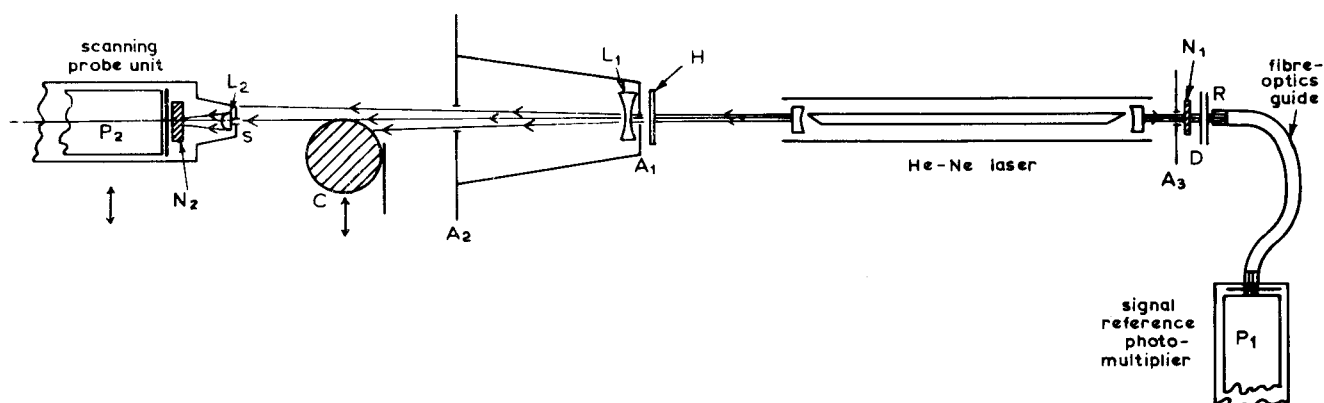* At u.h.f. the order of conductivity necessary to invoke this exception is never attained in ordinary terrain.

Fig. 14 - Optical arrangement for diffraction experiments (plan view)

4. LASER EXPERIMENTS

A series of optical diffraction experiments was carried out using the apparatus described in this Section. Polished aluminium cylinders are used to simulate hill profiles. The wavelength scaling is of the order of 10^6 : 1 so that a rounded hill with an effective radius of curvature of 5 km (3 miles) is simulated by a cylinder of radius 5 mm. From reflected-light experiments it appears that metals at optical frequencies also behave like lossy dielectrics. The modulus of the complex relative permittivity of aluminium at a wavelength of 589 nm is approximately 30, and the real part is again the larger term. This fortunate similarity between ordinary terrain at u.h.f. and metals at optical frequencies means that the simulation experiments should be realistic for all orientations of the plane of polarization.

Apart from verifying experimentally several major aspects of the rounded-hill theory, these experiments were largely directed towards investigating, in a quantitative manner, the shadow field of cylindrical crests with

(i) random-type surface roughness, and

(ii) non-constant crest curvature in the direction of propagation, e.g. flat-topped crests.

The basic requirement was for the generation of diffraction patterns, using cylindrical obstacles to simulate idealized hill profiles at u.h.f., and means for exploring and measuring the variation of the pattern intensities normal to the direction of propagation. A large part of the development of the apparatus was devoted to extending the range of reliable measurement into the very deep shadow region, where the differences in field amplitude due to variations in crest profile are greater.

An obvious choice for a monochromatic, spatially coherent source of radiation was a c.w. gas laser.

4.1. Apparatus

Fig. 14 shows the basic arrangement of the apparatus. A helium-neon gas laser*, with a confocal-type mirror cavity operating at a wavelength of 632·8 nm, was adjusted to emit a single-mode, narrow beam of light. The light was plane-polarized, by virtue of the Brewster end-windows, and a spatially-coherent beam of about 1 mm diameter was available from each end of the laser cavity.

One of the emerging beams was directed towards the diffracting obstacle through a small aperture A_1 in the screen. Immediately in front of this aperture was a half-wave, optical retardation plate H, made from a thin sheet of birefringent mica. The electric vector of the emerging radiation could then be set at any desired orientation by a suitable rotation of the retardation plate in its own plane. The diverging, cylindrical lens L_1 was inserted in order to increase the angular spread of the incident beam in a direction normal to the axis of the diffracting cylinder C. A virtual source position was thus located at the focal point of L_1, approximately 428 mm (6·75 $\times$ $10^5\lambda$) from the diffracting crest. Measurements of the beam cross-section, at the diffracting crest, showed the radial intensity pattern to be of approximately Gaussian form and large compared with the width of a Fresnel zone; thus the illumination of the obstacle was similar to that of a hill by a transmitting aerial. Before impinging on the obstacle crest the beam passed through a larger defining aperture A_2 in a screen which formed the end of a cone-shaped tunnel whose internal walls were blackened to reduce stray light.

For convenience, the diffracting cylinder C was mounted with its axis vertical so that diffraction occurred in a horizontal plane. Mechanical screw controls enabled it to be shifted horizontally and vertically with respect to the incident beam.

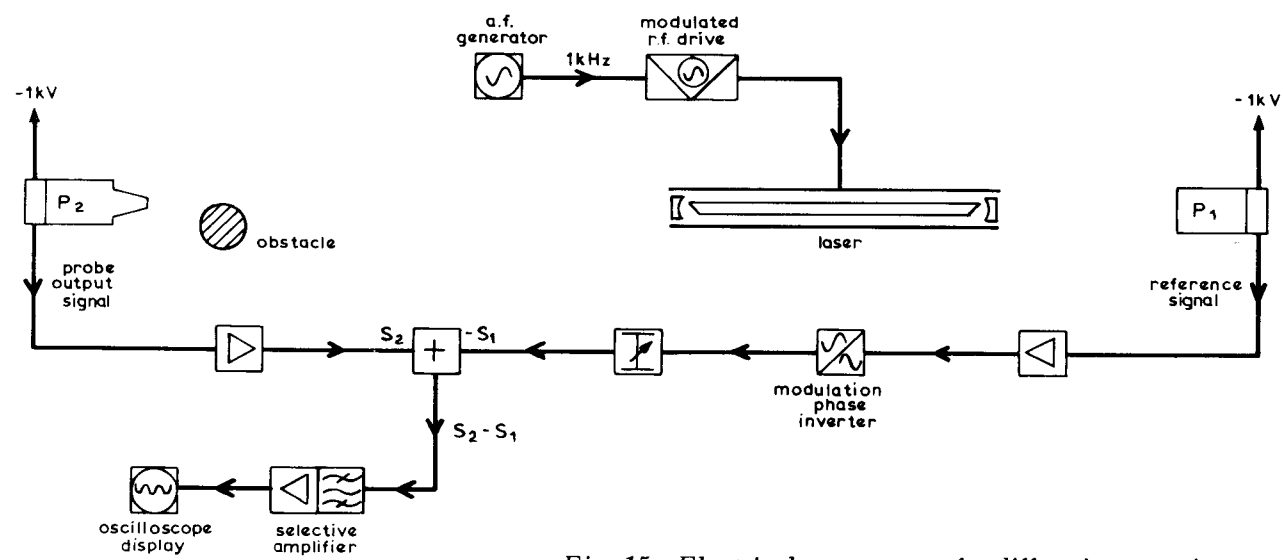* Manufactured by G.E. Bradley, Model 602, maximum output power approximately 1mW.

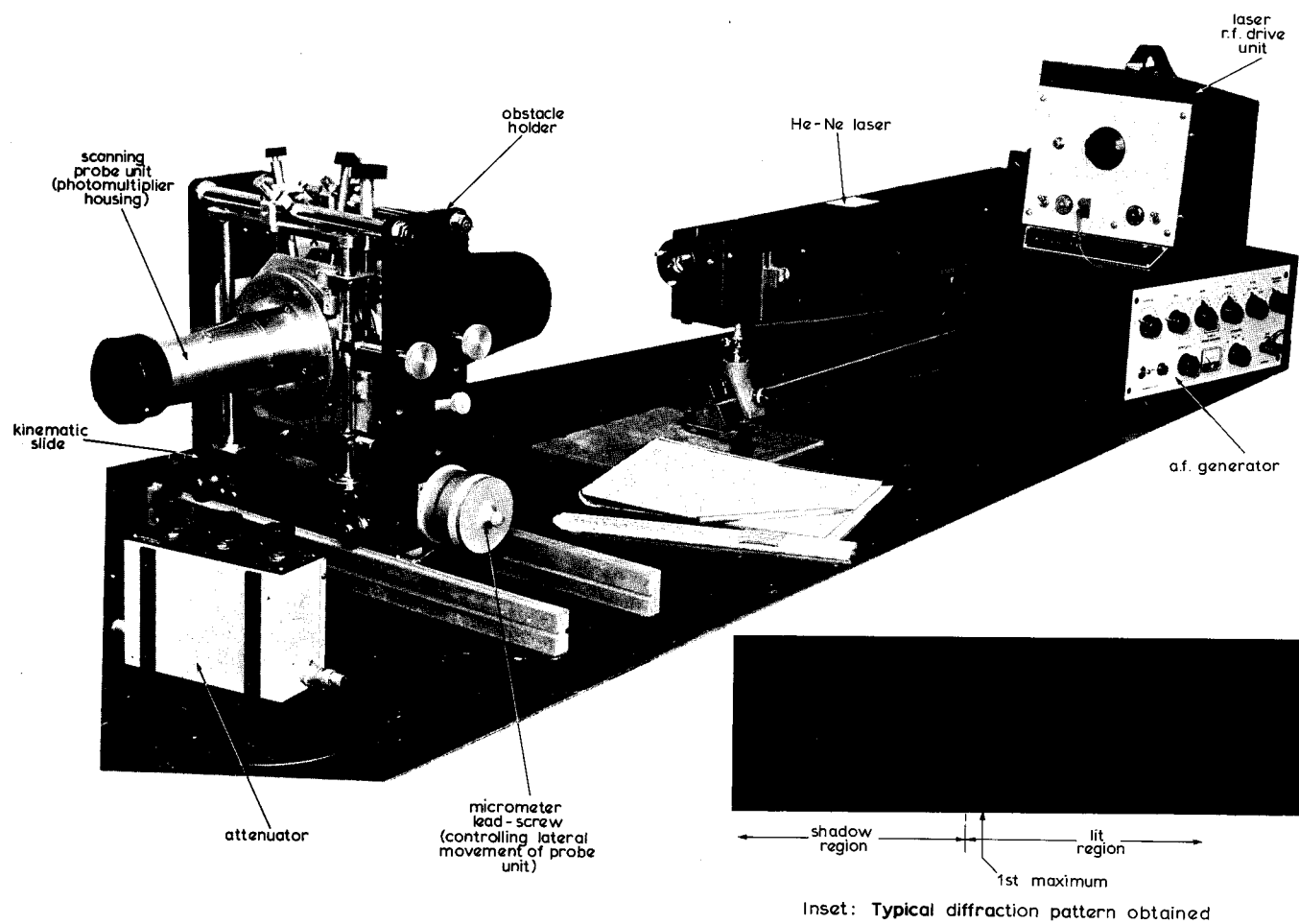Fig. 15 - Electrical arrangement for diffraction experiments

Inset: **Typical** diffraction pattern obtained

Fig. 16 - Apparatus for diffraction experiments
Inset: typical diffraction pattern obtained

The receiver probe consisted basically of a small slit (0·5 mm × 0·05 mm) in front of a sensitive, end-window photomultiplier (EMI type 9558A, tri-alkali). The slit aperture S was crudely imaged by the cylindrical lens L_2 on to the photo-cathode of the photomultiplier P_2, in order to reduce any local scanning of the cathode surface during a pattern measurement. A red (gelatine) filter was placed behind the slit aperture to absorb most of the non-lasing background radiation (spectral lines having shorter wavelengths) which accompanies the main beam. Also, a neutral-density filter N_2 was available to obtain a fixed amount of attenuation; this filter was easily retractable from the light path by means of an externally-operated lever.

The whole receiver unit was mounted on a kinematic slide, running horizontally and normal to the direction of propagation, and lateral scanning of the diffraction pattern was manually controlled by a micrometer lead screw.

The distance between the receiving slit-aperture and the diffracting crest was variable, but most of the measurements were made with a separa- of 25 mm $(4 \times 10^4\lambda)$

The light beam emerging from the other end of the laser cavity was used as an intensity reference, in order to overcome drifting of the laser output during pattern measurements. The background radiation was first removed by means of an aperture A_3, a metal-dielectric interference filter D and a red, gelatine filter R. A fibre-optics light-guide then led the filtered beam on to the photocathode of a second photomultiplier P_1, from which a reference signal was obtained. Provision was made for the insertion of a neutral-density filter N_1 to attenuate the reference beam if necessary.

4.2. Electrical Arrangement

The laser tube was r.f. excited by external electrodes coupled to a variable-power drive unit operating at 27 MHz. The r.f. drive was sinusoidally modulated at 1 kHz by the output of an a.f. generator, in order to intensity-modulate the light-beam at this frequency.

The a.c. signal outputs of the photomultipliers were amplified by similar transistor amplifiers (Fig. 15). The amplified signal originating from the reference photomultiplier P_1 was phase-inverted and then added to the amplified signal from the scanning photomultiplier P_2. The output of the combining stage, in effect a difference signal, was then fed to a frequency-selective amplifier tuned sharply to the modulation frequency, in order to improve the signal-to-noise ratio. The output of the tuned amplifier was displayed on an oscilloscope. A variable attenuator was inserted in the reference signal path as shown in Fig. 15.

The voltages for the dynode-chain circuits of the photomultipliers were obtained from a common, 1 kV E.H.T. supply.

Fig. 16 shows a photograph of the equipment and (inset) a typical knife-edge diffraction pattern, the maxima and minima of the pattern in the illuminated region being clearly demonstrated.

4.3. Measurement Procedure

It was required to determine the basic pattern function $|E(x)/E_0|$, where $E(x)$ is the field amplitude at a point in the shadow distant x from the geometrical shadow boundary (Fig. 17), and E_0 is the free-space field amplitude (taken here as the field amplitude near the origin $x = 0$ with the obstacle removed). It is perhaps worth mentioning that the signal current output of a photomultiplier is proportional to $|E|^2$, i.e. it measures the time-averaged power, but for our measurements this simply means that a 2 dB variation in signal current is equivalent to a 1 dB variation in field amplitude.

It was found more convenient, however, to measure $|E(x)/E_{max}|$, where E_{max} is the field amplitude at the first maximum of the interference ripple on the illuminated side (see Fig. 17). At the end of the scanning run the receiving probe was returned to the position of the first maximum, which was easy to locate precisely, and the ratio $|E_{max}/E_0|$ measured by simple removing the obstacle.

It was assumed, in referring the results to an origin on the shadow boundary, that the position of the first maximum is largely independent of the curvature of the diffracting crest. This assumption is retrospectively justified by the agreement obtained between theory and experiment.
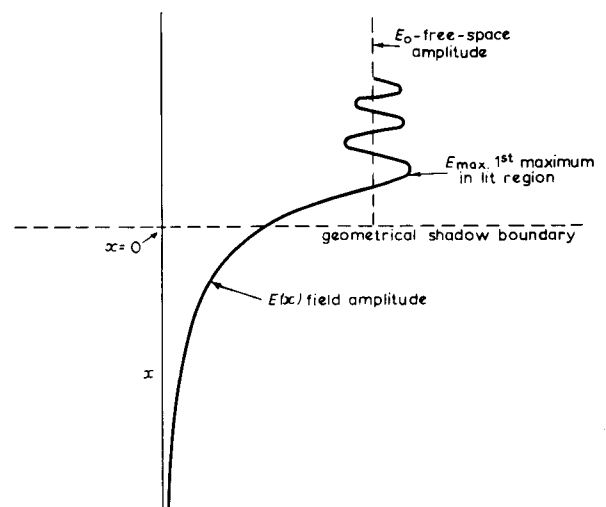

E_0 - free-space amplitude

E_{max}. 1st maximum in lit region

geometrical shadow boundary

$x = 0$

$E(x)$ field amplitude

x

Fig. 17 - Typical form of the diffraction pattern

The axial distance between the receiving slit-aperture and the diffracting crest was measured with a travelling microscope.

Apart from the initial optical alignments, and the critical adjustment of the laser mirrors to obtain a single, axial-mode beam, the measurement procedure was as follows:

The first maximum of the diffraction pattern was located by a lateral exploration of the receiving probe. In this region, where the pattern intensity is greatest, the neutral-density filter N_2 (Fig. 14) was always in position, reducing the intensity by a factor of 10^{-3} to prevent overloading the photomultiplier. The attenuator controlling the amplitude of the reference signal originating from P_1 was set to zero attenuation. Then, by inserting suitable neutral-density filters in the reference beam followed by a fine adjustment of the amplifier gain, a null balance was obtained, this condition being indicated by a straight-line trace on the oscilloscope c.r.t. Next, using the variable attenuator, the reference signal was reduced by a suitable amount (the usual interval was 5 dB) and a null-balance re-established by moving the receiving probe further into the shadow. The probe position was then read and recorded, the attenuation increased by a further amount and the procedure repeated. At the shadow position where $|E(x)/E_{max}| \approx -30$ dB, the neutral-density filter N_2 was retracted and, after resetting the attenuator and rebalancing, step-by-step measurements continued again until $|E(x)/E_{max}| \rightarrow -60$ dB, which was about the limit set by noise.

4.4. Diffracting Models

The model obstacles used to simulate various hill profiles were constructed from polished aluminium cylinders of various radii of curvature and from machined slabs. For example, a 10 mm radius cylinder was required to simulate a 6·4 km (4 mile) radius hill crest of constant curvature at u.h.f. Double-hump profiles were constructed by abutting cylinder segments, and flat-top profiles by stretching polished aluminium foil over double-hump models.

Initial experiments were carried out using a polished glass cylinder of optical quality coated with a vacuum-evaporated metal film. Gold, silver and aluminium coatings were used but no significant differences in the shadow field strength were found between these and polished bulk aluminium, even though the latter is known to have a thin surface layer of aluminium oxide*.

5. ROUGHNESS SIMULATION AND MEASUREMENT

Random-type surface roughness was simulated by wrapping abrasive papers around the aluminium

cylinders used for the model hills. These papers, which are available in many grades, consist of particles of silicon carbide or emery partially embedded in a resinous layer sticking them to the base. A microscopical examination of the structure of these papers showed the surface to appear as an irregular distribution of many-facetted protuberances, largely restricted in their sizes according to the particular grade of paper; the larger the mean size of the protuberances the greater is their mean separation. Described in this way, such a surface structure is not unrepresentative of the type of roughness encountered with real terrain, for example that of a built-up populated area.

Four grades of abrasive paper were selected to obtain a suitable range of surface roughness. In order to vary the roughness of the surface only and not its physical properties, the papers were first coated with a thin layer of aluminium in a vacuum-evaporation plant.

Various practical methods were considered for obtaining a representative graphical record of the surface height variations for each grade of paper. A photometric method was developed, using a recording densitometer to scan a dyed-resin replica of the surface structure, but this failed to deal adequately with the finer grades of abrasive paper. For the latter grades, height-profile recordings were obtained from a Talysurf* surface measuring instrument in which a fine diamond stylus is dragged across the surface and vertical deflections of the stylus are transduced, amplified and recorded.

Portions of the actual profile traces recorded, which are typical of the surface height variations of the four grades of paper used in the diffraction experiments, respectively, are grouped together in Fig. 18. The horizontal magnification is 100, and the vertical magnification 2000 except for the coarsest sample (d), for which it is 1000. Owing to the finite dimensions of the stylus tip, some of the finer structures believed to exist in the smoothest sample (a) are not fully resolved.

By sampling the recorded profile traces, the r.m.s. deviation of surface height from the mean height was estimated for each grade of paper. In addition, autocorrelation functions were derived and these indicated that the distributions of the surface irregularities were substantially random, although not completely since some periodicity was observed.

Table 1 summarizes the roughness characteristics of the four samples referred to in Fig. 18. The average spacing and width of the protuberances were estimated on the basis of direct measurements using a travelling microscope. The average height of the structures and the r.m.s. deviation of surface height were determined from the profile traces. The

---

* The oxide layer thickness is believed to be less than 10 nm.

* Precision surface-measuring equipment manufactured by Rank, Taylor-Hobson, Leicester.

last column in Table 1 is included to aid a comparison with real terrain at u.h.f. by supposing that $\lambda = 0.46$ m (1.5 ft). The accuracy of the statistical measurements given in Table 1 is believed to be better than $\pm 20\%$.
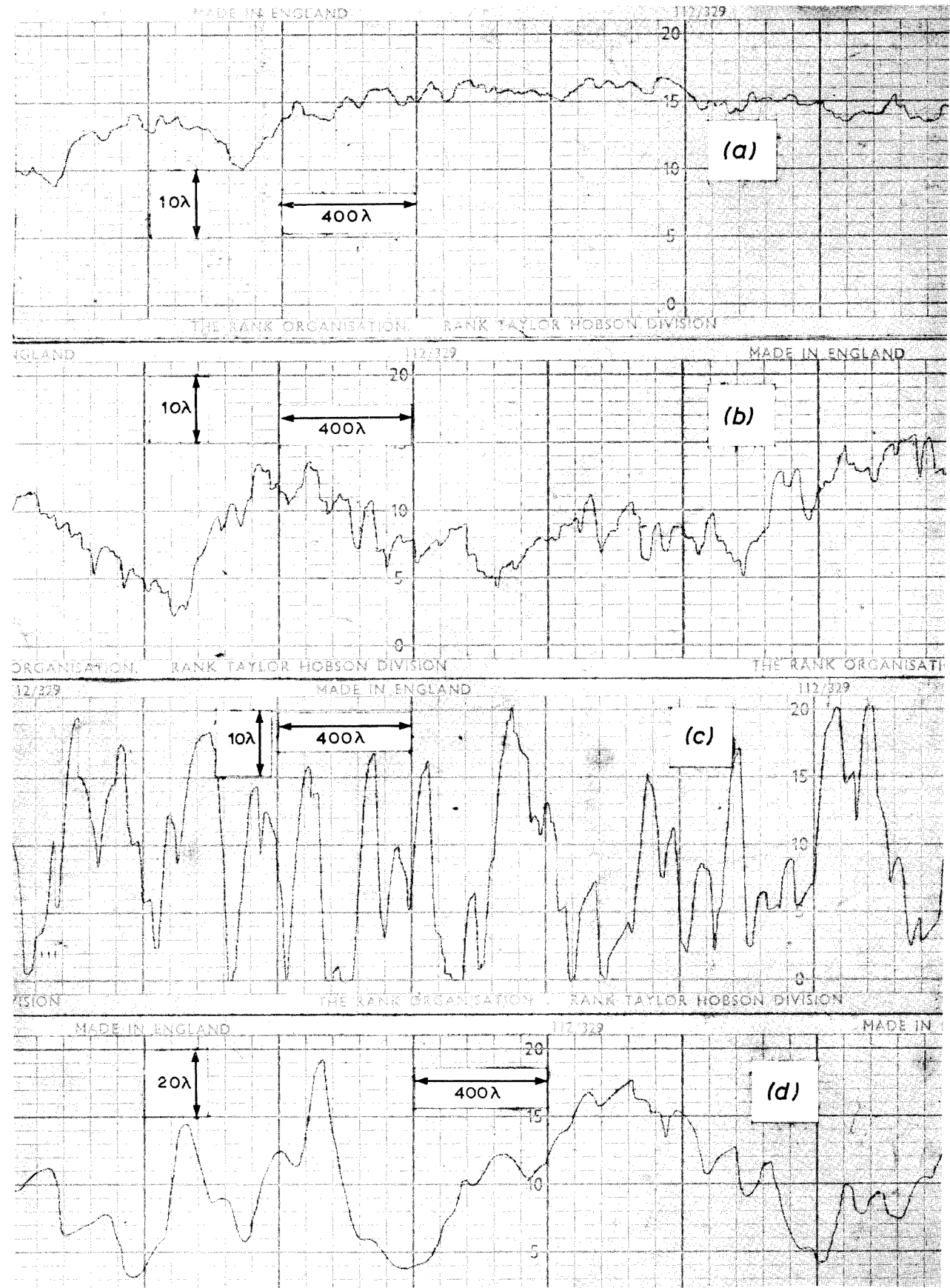
Fig. 18 - Height profiles of four abrasive papers

TABLE 1

Roughness Characteristics of Surfaces

Sample	Average dimensions of structures			R.M.S. deviation of surface height	Average No. of structures per acre* (λ = 0.46 m) (1.5 ft)
	Height	Width	Spacing		
(a)	5λ	<15λ	<40λ	1.7λ	>12.5
(b)	9λ	25λ	55λ	4λ	6.4
(c)	25λ	45λ	100λ	11λ	2
(d)	40λ	90λ	200λ	18λ	0.5

* 1 km^2 ≈ 250 acres

Fig. 19 - Field-strength variations: smooth cylinders and knife-edges

x — — x R = <5λ (razor-blade edge)

Measured { -o- — -o-R = 4000λ, smooth cylinder

Values { ▲-----▲ R = 16,000λ, smooth cylinder

-▣- - -▣ R = 63,000λ, smooth cylinder

———— Theoretical, perfect knife-edge

6. EXPERIMENTAL RESULTS

The results given in this Section refer to measurements made with horizontally-polarized radiation (electric vector perpendicular to the plane of incidence or, alternatively, parallel to the cylinder generators).

6.1. Crest Profiles of Constant Curvature

6.1.1. Smooth Surfaces

These were represented by polished aluminium cylinders of circular cross-section but with various radii of curvature, and were used mainly to test the validity and accuracy of the experimental arrangement, since the theoretical solution for this model is well established (see Section 3).

The lower curves in Fig. 19 show the variation of the relative field strength with shadow position, measured at a fixed distance from the diffracting crest, for three cylinders whose radii of curvature were 2·5 mm (4000λ), 10 mm (16000λ) and 40 mm (63000λ) respectively. The geometry of the arrangement is shown inset on the figure. The shadow position is specified in terms of the Fresnel parameter, v, so that $v = 0$ represents a point on the geometrical shadow boundary and $v = -1·22$ is assumed to the the position of the first maximum on the illuminated side of the boundary.

The upper broken curve in Fig. 19 is the measured result for the shadow field of a stainless-steel razor blade, which was included to represent a smooth crest of vanishing radius of curvature. For comparison, the upper full-line curve is the well-known theoretical result for a perfect knife-edge.

It will be seen from Fig. 19 that the field strength, at a given point in the shadow, decreases as the crest curvature decreases. Also, the slopes of the curves demonstrate the theoretical prediction that obstacles with diffracting crests of shallow curvature cast sharp shadows.

The measured result for the razor blade model is seen to diverge slightly from the theoretical variation for a perfect knife-edge, and this is believed due to the finite radius of curvature of the blade crest, which is probably of the order of two or three wavelengths.

The validity of the theoretically-derived excess-loss function (Section 3.3) for crests of constant curvature is of particular interest, and Fig. 20 shows the measured diffraction loss in excess of that of a perfect knife-edge as a function of the parameter r. Each plot point in a group on the figure refers to a particular radius of curvature and the full-line curve is the theoretical excess-loss

function (for $D/d_0 = 25$) given earlier. The agreement is seen to be generally good over the range investigated $r = 0$ to 2. At $r = 0$, the measured excess-loss is almost zero for the small-radius cylinder but approaching 1 dB for the largest cylinder. This is in accord with theory because the basic excess-loss near $r = 0$ is slightly but significantly dependent on the parameter D/d_0, as may be seen from Fig. 7. Although D was kept fixed in the experiment d_0 is proportional to the cylinder radius and therefore variable; the D/d_0 values for the three cylinders, are shown on Fig. 20.

6.1.2. Rough Surfaces

Samples of each of the four grades of abrasive paper, described in Section 5, were wrapped in turn around each of the three smooth cylinders and diffraction measurements carried out on each of the twelve different combinations of cylinder radius and surface roughness thus obtained. At least two shadow-field variations were measured for each combination, using a different region of the rough surface for each run.
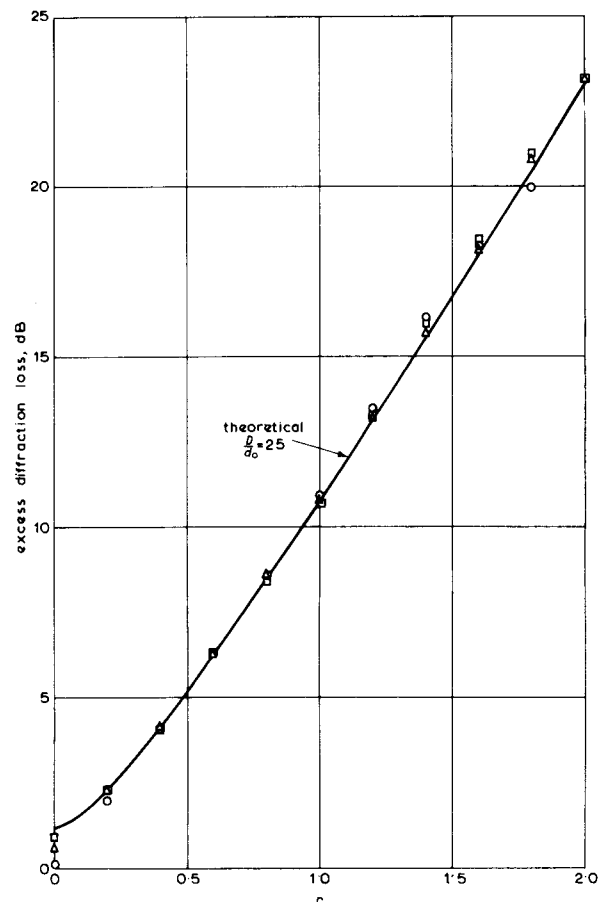

Fig. 20 - Basic excess-loss function: comparison with measurement

Measured Values
{ o $R = 4,000λ$, $D/d_0 = 222$
  ∆ $R = 16,000λ$, $D/d_0 = 89$
  □ $R = 63,000λ$, $D/d_0 = 35$
——— Theoretical $D/d_0 = 25$
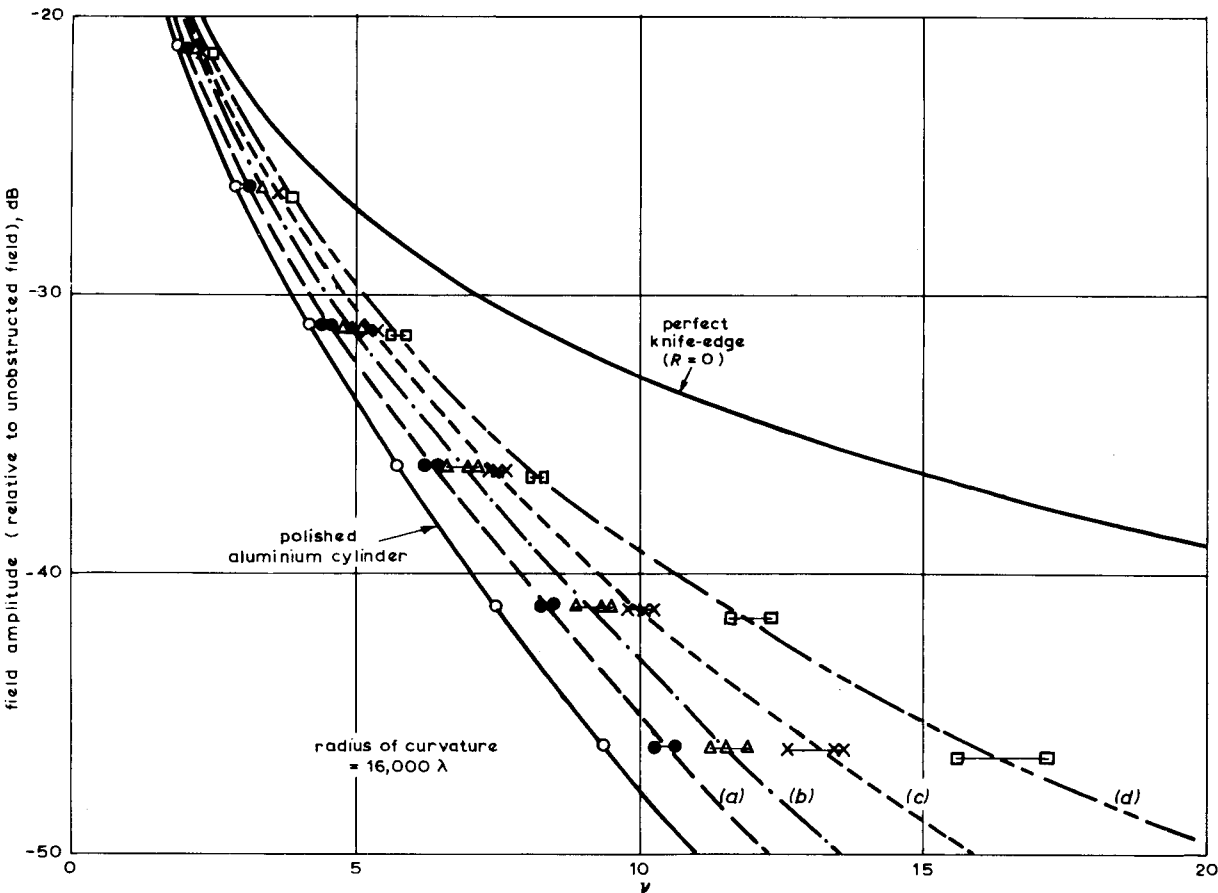
Fig. 21 - Effects of surface roughness on the shadow field

	⊖————⊖ Smooth surface, polished aluminium cylinder
	●———● Rough surface, sample (a)
Measured	▲——▲ Rough surface, sample (b)
Values	✳——✳ Rough surface, sample (c)
	⊟——⊟ Rough surface, sample (d)

——————— Theoretical, perfect knife-edge
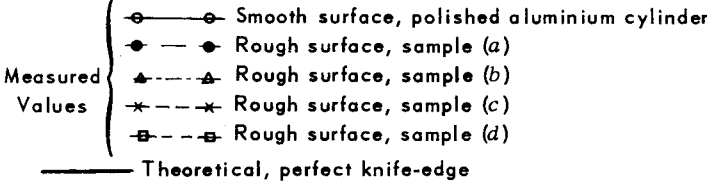
The detailed results for one of the cylinders (radius of curvature = 16,000λ) are given in Fig. 21, where the measured field variations are given for the four rough surfaces and the smooth surface. It is clear from this Figure that increasing the surface roughness of the diffracting crest has the effect of brightening the shadow, i.e. increasing the field amplitude at every point.

From all the results, the representative excess-loss functions were derived for each of the cylinder radii/surface-roughness combinations. These were averaged with respect to cylinder radius and yielded the results shown in Fig. 22. The upper full-line curve refers to the smooth (polished) surface. The plot points grouped around the curve (c) are the actual excess losses obtained with the three cylinder radii for the roughness sample (c), at several r-values. From the relatively small spread of these points, it would appear that the single-parameter dependence of the excess-loss function, which is an interesting feature of the behaviour of smooth diffracting crests of constant curvature, is

not destroyed when the surface is roughened.

Combining the roughness measurements given in Table 1 earlier with the data of Fig. 22, we can obtain a quantitative relation between the r.m.s. deviation of surface height and the increase in field strength with respect to a perfectly smooth crest of constant curvature. This relation is shown in Fig. 23, for two values of the parameter r, where smooth curves have been drawn through the measured plot points. A feature of this relation is the asymptotic trend for large values of r.m.s. height deviation. This is to be expected if it is accepted that the field strength (for horizontal polarization) can never exceed that given by a single, perfect knife-edge. In fact, however, the single knife-edge limit was not reached, even if very coarse grades of abrasive paper were used, which suggests the possibility that the upper limit is closer to that set by a double or multiple knife-edge configuration.

The rough surfaces considered so far were randomly irregular in two dimensions and statis-

tically isotropic. A less realistic but simpler representation of a perfectly-rough cylindrical crest is a stack of razor blades whose edges are mutually parallel and, in the direction of propagation, lie on a circular arc of a given radius. Diffraction by a model of this kind was investigated experimentally. It was constructed from 13 razor blades, spaced 0.75 mm (1200λ) apart, with edges describing a circular arc of 40 mm (63000λ) radius. The relative field-strength variation as a function of v is shown in Fig. 24, and refers to the geometrical arrangement inset on the figure. For comparison, the corresponding measured variations for a (continuous) smooth surface, a randomly-rough surface (sample (d)) and a perfect knife-edge are also displayed. It will be seen that field strength in the shadow of the randomly-rough surface is somewhat greater than that of the razor blade model.
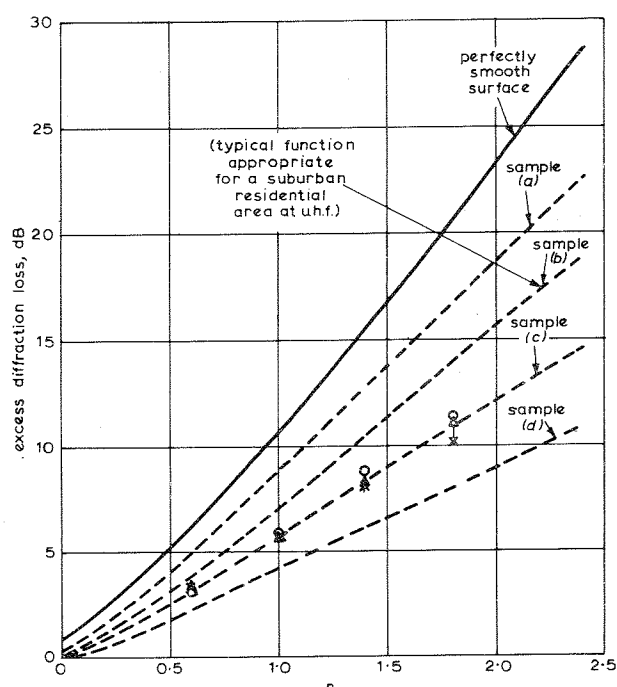

Fig. 22 - *Representative excess-loss functions; rough-surface samples*

Excess-loss values for sample (c) $\begin{cases} \times & R = 4000\lambda \\ \circ & R = 16,000\lambda \\ \triangle & R = 63,000\lambda \end{cases}$

6.1.3. Remarks on the Application of the Results

In order to apply the rough-surface results in u.h.f. prediction work it is necessary to establish the effective radius of curvature of the crest and, in addition, make some assessment of the terrain roughness over the crest. The former can be obtained with sufficient accuracy by interpolating the ground profiles derived from ordnance survey maps. The roughness assessment, on the other hand, is not so straightforward. If the terrain over the hill crest or ridge is sparsely populated moorland, then the

smooth-surface excess-loss function (Fig. 9) is appropriate and the experimental results indicate that this can be applied with confidence when the crest curvature is constant or only slowly varying. For built-up populated terrain, with an irregular distribution of buildings, trees etc., a more appropriate excess-loss function than that for perfectly smooth terrain can be found if an estimate of the r.m.s. deviation of surface height can be obtained.
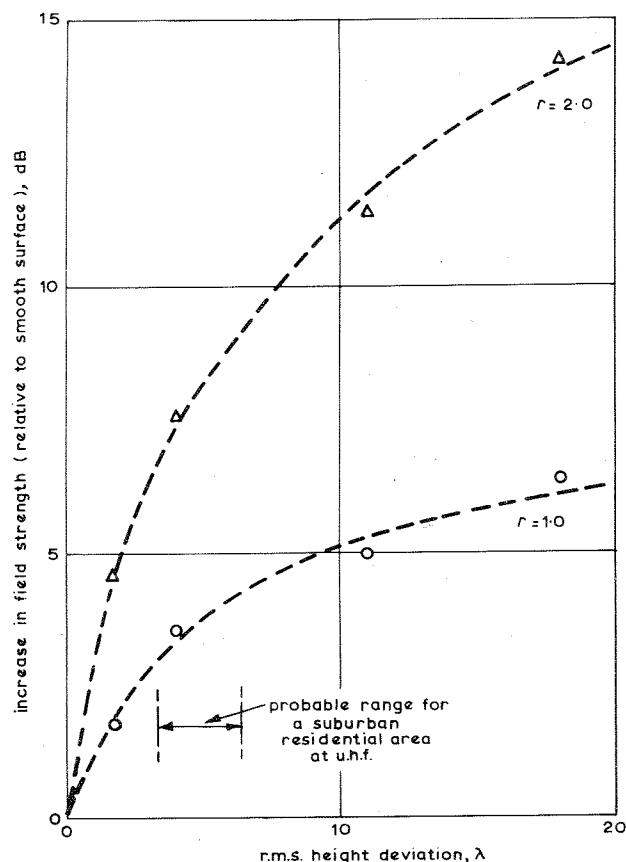

Fig. 23 - *Variation of shadow field strength with random-type surface roughness*

As an example, suppose that we are interested in the diffraction loss over a gently curved hill of approximately constant curvature in the direction of propagation. Let us assume that the hill is part of a suburban residential area and that there are, on average, two houses 9 × 6 m, × 9 m high (30 ft × 20 ft, × 30 ft high), and two trees 4.5 × 4.5 m, × 9 m high (15 ft × 15 ft, × 30 ft high) per acre* of surface. The r.m.s. deviation of surface height is calculated to be approximately 1.8 m (6 ft) which for u.h.f. broadcasting corresponds to a deviation, in terms of wavelength, of 3λ to 5λ. This probable range for a suburban residential area is indicated on Fig. 23, where it will be seen that, at $r = 2$, an increase of field strength relative to the perfectly smooth hill of the same mean curvature of approximately 8 dB is predicted. Further, an appropriate excess-loss
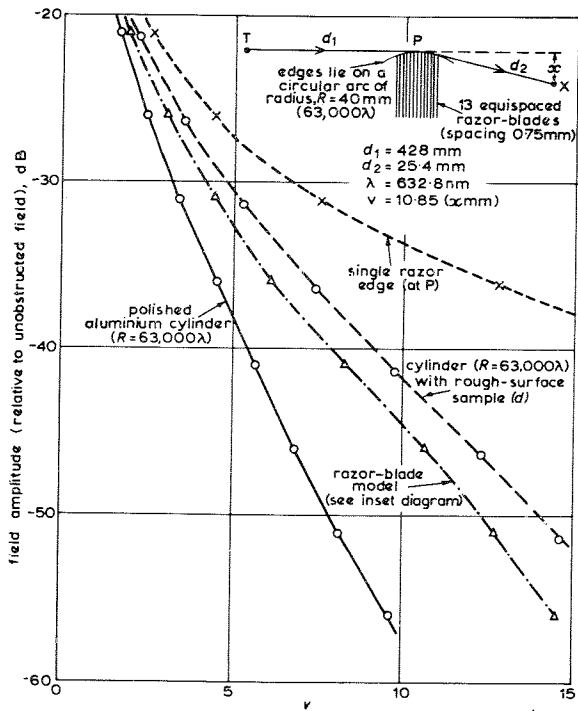
* 1 km^2 $\approx$ 250 acres.

Fig. 24 - Shadow field variations: results for razor blade model compared with rough and smooth cylinders

function for this category of terrain structure would be close to sample (b) in Fig. 22.

One or two other broad categories of terrain structure may be classified in this manner, e.g. dense woodland. Overall, this procedure should lead to more accurate loss predictions than are possible by always applying the smooth-surface result.

Finally, it should be pointed out that when there are just one or two isolated but large structures on the hill, which is otherwise smooth, these may form the major diffracting ridges along a given profile. Clearly, such structures cannot be ignored on the grounds that the r.m.s. deviation of surface height is barely increased by their presence. For example, a single line of trees, forming a ridge on the hill top which runs across the direction of propagation, must be treated as a diffracting edge in its own right. An idealized case of this problem is examined in Section 6.2.2 below.

6.2. Double-Hump Profiles

Propagation over two rounded hills or ridges in tandem is included under this heading, but the situation where the two diffracting crests are close together was examined experimentally in greater detail. The profile then consists of two arcs in tandem separated by a cusp-shaped valley or depression. In the experiments the two arcs constituting the profile of the model were circular.
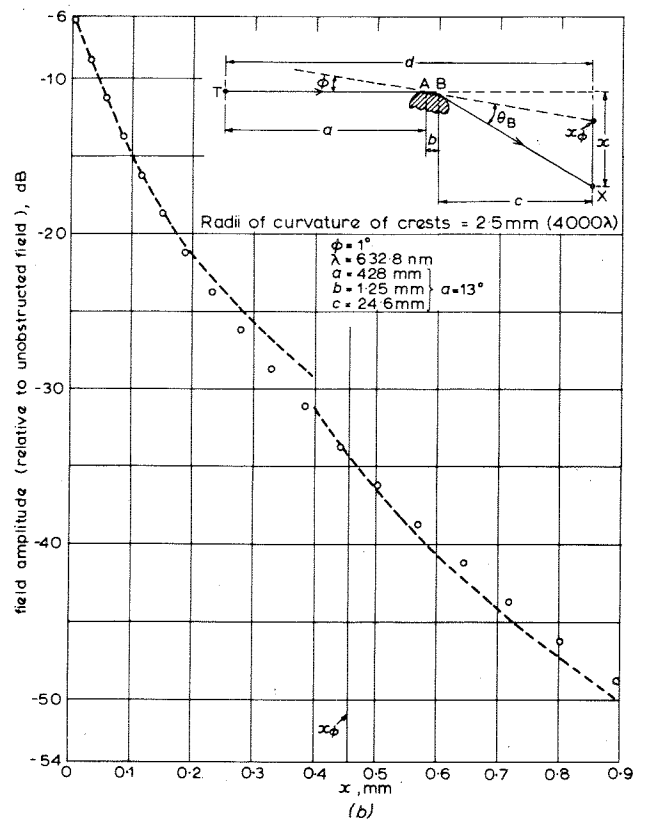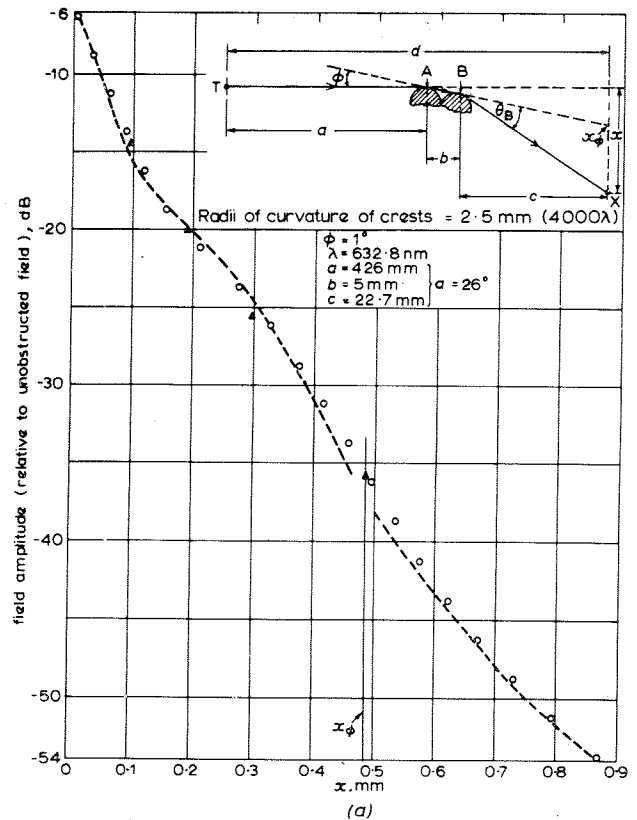

Fig. 25 - Shadow field variation

(a) Wide-spaced double-hump, $\alpha = 26°$
   o Measured   ---- ▲ } calculated

(b) Close-spaced double-hump, $\alpha = 13°$
   o Measured   ----- calculated

6.2.1. Crests with Equal Curvature

The models were constructed from two polished aluminium cylinders (or two segments of them) having the same diameter and aligned with their axes parallel.

Before giving some results of the double-hump experiments it is worth defining what is meant by 'close-spacing' when applied to double crests. A dimensionless parameter which arises in the theory of diffraction by two knife-edges in tandem[13] is $\alpha \equiv \tan^{-1}(bd/ac)^{1/2}$, where a, b, c and d are the distances shown on the diagram inset on Fig. 25(a). The parameter α, whose value lies in the range 0 to $\pi/2$, is dependent only on the relative spacing of the diffracting edges (or crests) from each other and from the transmitter and receiver. Here the crests will be regarded as 'close-spaced' when α is less than 20°.

The results of two double-hump experiments are given in Figs. 25(a) and 25(b), which refer to $\alpha = 26°$ and $\alpha = 13°$ (close-spaced) respectively; the radius of curvature of the crests was 2·5 mm (4000λ) in both experiments. The angle ϕ between the common tangent to the crests and the transmitter horizon was fixed at 1° in both experiments (ϕ is considered positive if the transmitter lies below the common tangent). The open-circle plot points show the measured variation of $|E(x)/E_0|$ as the receiver moves from a point on the shadow boundary ($x = 0$) into the shadow region. The dashed-line curves in Figs. 25(a) and 25(b) are the expected variations in field strength, respectively, and were calculated in the following manner:

(i) The arrangement was treated as two perfect knife-edges in tandem, situated at A and B (Fig. 25), and the field–strength variation calculated by the method described in Section 3.4.

(ii) The extra attenuation due to the finite curvature of the crests was deduced by imagining that a string running over the crest(s) and joining the transmitter T to the receiver X, is pulled taut. Now when X is in the region $x = 0$ to $x = x_\phi$ (Fig. 25(a)) the string has two straight portions and the excess-loss was simply deduced as for a single crest having a curvature equal to that of obstacle A. However, when X is in the region where $x > x_\phi$ double diffraction occurs and our imaginary string will have three straight portions, intersecting at angles ϕ and θ_B. A further attenuation was then allowed for the curvature of crest B, where the excess-loss parameter was assumed proportional to θ_B.

The discontinuities in the dashed-line curves of Figs. 25(a) and 25(b) arise because the double

knife-edge contributions in each case were calculated using one or more approximate methods[16,18], and different methods were used for the ranges $0 < x < x_\phi$ and $x > x_\phi$, approximately. Further, some of the apparent discrepancy between the calculated and measured values in the region $x \approx x_\phi$, is believed due to the partial failure of the approximate methods in this critical region, where both crests (A and B) lie on the receiver horizon. In Fig. 25(a) the solid triangle points are predicted values obtained when the double knife-edge contribution is calculated using Millington's more rigorous method[13].

It is clear from the good agreement obtained that the above method of treating the double-hump situation is valid for both close-spaced and wide-spaced crests. A secondary feature, indicated by the experimental results, is that if double diffraction occurs ($x > x_\phi$) a close-distance correction (Section 3.3) should not be applied when calculating the curvature loss due to crest A even though the two crests may be close together.

Finally, if one or both of the crests are randomly rough a more appropriate basic excess-loss function can be used, as outlined in the previous Section.

6.2.2. Crests with Unequal Curvatures

A double-hump situation was investigated in which the crest curvatures were widely different. The model was obtained by laying a fine wire of radius 0·0127 mm (20λ) on a polished cylinder of radius 10 mm (16000λ); the axes of the wire and cylinder were set parallel.

Diffraction measurements were carried out for the two arrangements shown in Fig. 26 by the diagrams A and B respectively, together with the measured relative field-strength variations as a function of the shadow position, at a fixed distance from the larger cylinder. The upper and lower full-line curves are the theoretical variations obtained for single, isolated crests whose radii of curvature are 20λ and 16000λ respectively, and are included for comparison with the double-hump measurements (curves A and B).

The general behaviour of the shadow field in this situation is now apparent. In arrangement A the sharper crest is dominant and the field strength at first diminishes as if that crest existed in isolation. As the receiver horizon gets closer to the blunt crest, however, the amplitude of the radiation received directly becomes comparable with that of the component reflected from the intervening blunt crest; these components interfere and generate the characteristic, spatial perturbation of field strength seen in Fig. 25 (curve A). Finally double diffraction occurs ($v > 17$), the interference ripple ceases
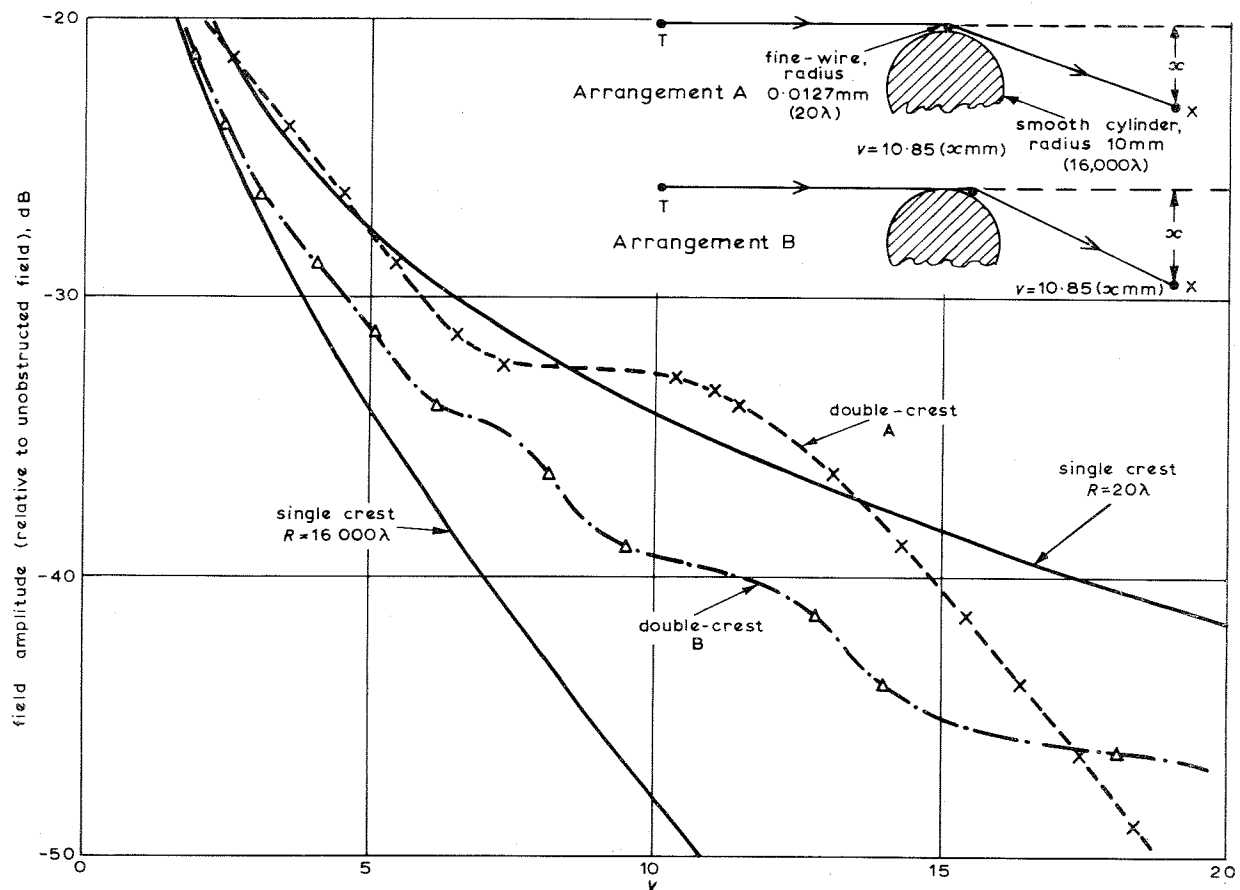
Fig. 26 - Shadow field variation: double-hump configurations with unequal crest curvatures

Measured { X— — —X arrangement A
            A— - —A arrangement B

———— Theoretical, single crests

and the field diminishes at a rate governed by the radius of curvature of the blunt crest.

In the other configuration B, where both crests lie on the fixed transmitter horizon, the field strength initially follows a variation similar to that of the blunt crest in isolation. As the receiver moves deeper into the shadow field, the sharper crest becomes dominant and controls the average rate of field-strength attenuation. In this shadow region, the overall reduction in field strength, relative to the sharper crest in isolation (which approaches 6 dB) is due to the presence of the blunt crest on the transmitter side, while the spatial perturbation of the field strength is due to the presence of the blunt crest on the receiver side. Eventually, although beyond the range shown in Fig. 26, the blunt crest defines the receiver horizon and (as in configuration A) the rate of attenuation increases according to its curvature.

Similar close-coupling effects must be expected in real-terrain situations where a single, large obstacle lies on the crest of a rounded hill. At u.h.f., for example, the idealized model investigated here would correspond to, say, a long ridge of trees about 20 m (60 ft) wide by 20 m (60 ft) high situated

on a smooth hill-crest with a radius of curvature of 7 or 8 km (4 or 5 miles).

6.3. Crest* Profiles of Varying Curvature

Two types of model were used for these experiments and Fig. 27 shows their sections in the plane of propagation. The flat-top type, Fig. 27(a), was constructed by stretching strips of thin aluminium foil over the double-hump models used previously. The square-top type, Fig. 27(b), was machined from solid aluminium and the flat faces hand-polished.

6.3.1. The Flat-Top Profile

Referring to Fig. 27(a), the flat-top profile has a portion AB of zero curvature which separates two regions of finite curvature. The curvature along the crest profile thus has a sudden transition in value in the neighbourhood of the points A and B.

From a diffraction point of view, one way of regarding the flat-top profile (depending on the orientation of the flat portion with respect to the

* In this Section the term 'crest' is defined more specifically as that portion of the obstacle profile between the tangent points of the transmitter and receiver horizons.

transmitter/receiver horizons) is as a single crest of constant curvature not completely isolated from the transmitter/receiver. Alternatively, it may be regarded as a double-hump system with the trough between the humps filled in. For example, if the receiver is at the point X_1 (Fig. 27(a)) the actual crest profile has constant curvature but the flat-top portion of the obstacle profile can be expected to influence the field at X_1, especially if it has appreciable length compared with TA or AX_1. Again, if the receiver is at the point X_2, the aperture above B, and hence the field at X_2, must be significantly influenced by the flat portion between A and B.
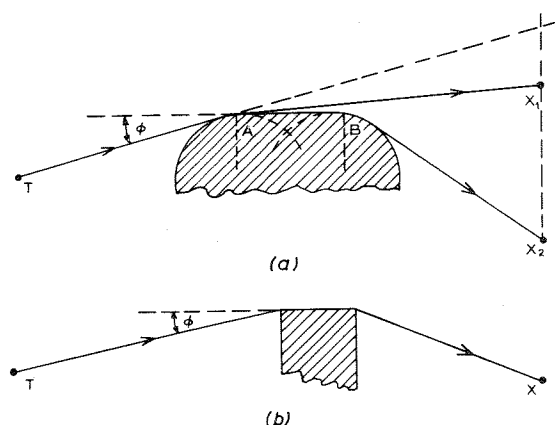

(a)

(b)

Fig. 27 - Geometry of two varying-curvature profiles
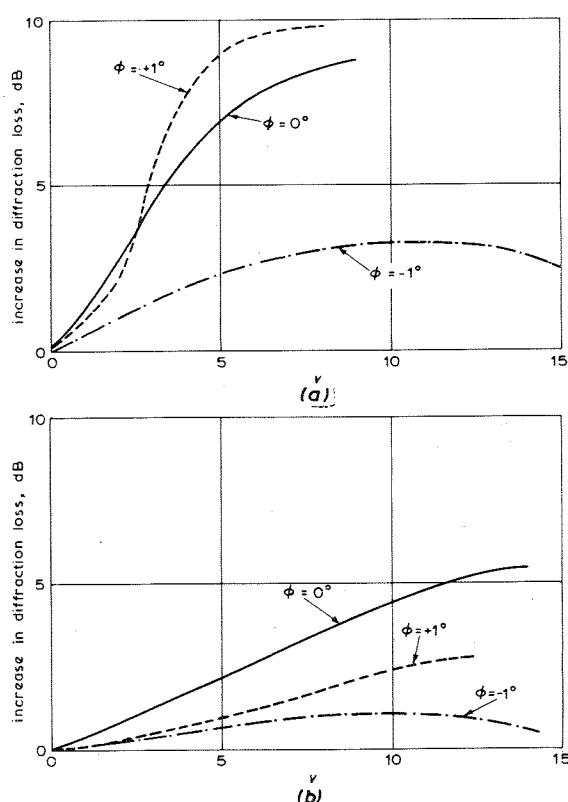
(a) Flat top   (b) Square top (thick slab)

(a)

(b)

Fig. 28 - Measured increases in diffraction loss of the flat-top profile over the double-hump profile

(a) $\alpha = 26°$ (b) $\alpha = 13°$

The main part of the investigation was to determine the effects on the shadow field strength of filling-in the space between the crests of a double-hump profile to form a flat-top profile. Several double-hump models, which had been measured previously, were converted to flat-top form and the diffracted fields measured again under the same conditions. It was found that the flat-top profile always casts a sharper shadow than the corresponding double-hump. This may be seen from the results for two models with different crest spacings shown in Fig. 28(a) and 28(b), respectively, where the increase in the diffraction loss of the flat-top profile with respect to that of the corresponding double-hump profile is plotted against the Fresnel parameter v, which defines the position of the receiver in the shadow, for three fixed values of ϕ (Fig. 27(a)). The curves in Fig. 28(a) refer to the crest spacing for which $\alpha = 26°$, and those in Fig. 28(b) to a closer spacing where $\alpha = 13°$ (see Section 6.3.1). The radii of curvature of the crests, or of the rounded portions of the profile in the case of the flat-top models, was 2.5 mm (4000λ).

From these results it is evident that the excess-loss of field strength due to the flat portion of the obstacle profile depends critically, and in a complicated manner, on the three parameters α, v and ϕ. As the receiver moves from the just-line-of-sight position ($v = 0$) into the shadow, the increase in loss is at first small but becomes of considerable magnitude deeper into the shadow, especially if α is large. The greatest diffraction losses are obtained when the flat-top portion is part of the actual crest profile, i.e. for $\phi \geqslant 0$. If ϕ is negative, the increase in loss appears to reach a broad but definite maximum.

Some general conclusions can be drawn from the various experiments which are relevant to propagation over real-terrain profiles of this kind at u.h.f.:

Where the profile of the diffracting obstacle in the direction of propagation contains a flat portion, its effect can be neglected without serious error providing that its length b is such that $\alpha = \tan^{-1}(bd/ac)^{1/2}$ is less than about 15° and v is not too large, say $v<6$. The obstacle may then be regarded as a straightforward double crest and treated accordingly.

Some account should be taken of any smooth, reasonably flat portion of the obstacle profile, however, if its length is such that α is greater than about 25° and it forms the major part of the actual crest. In this case, the contribution to the diffraction loss made by the curved portions of the crest profile is expected to be small. Consequently, it is suggested that the flat-top profile can then be sufficiently well represented by a square-topped thick slab with the same value of α, for which a method of calculating the diffracting loss has been derived and which is discussed below.
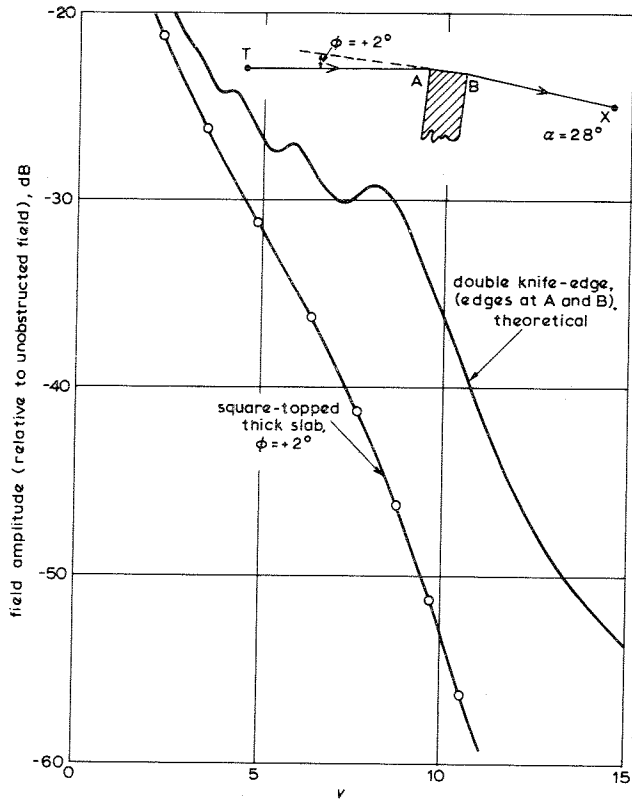
(a)
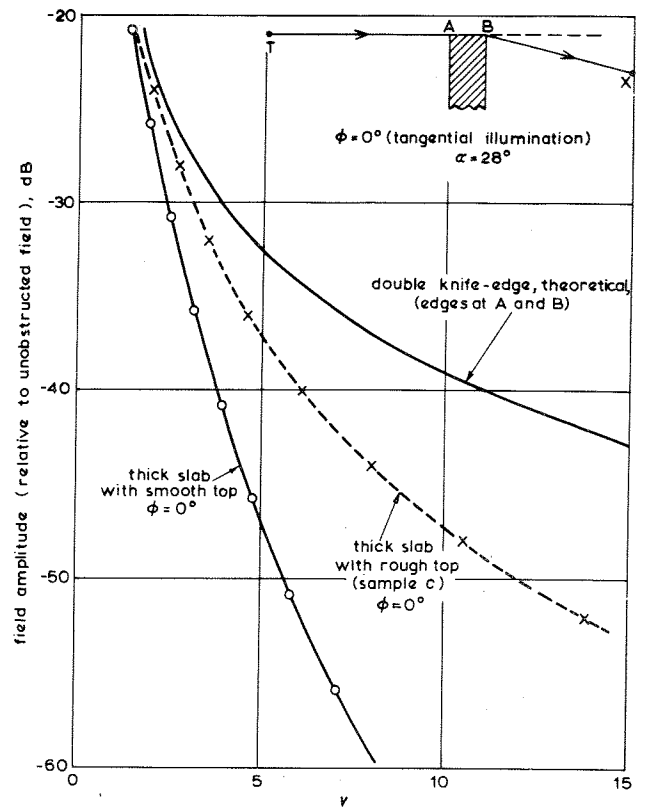
(b)
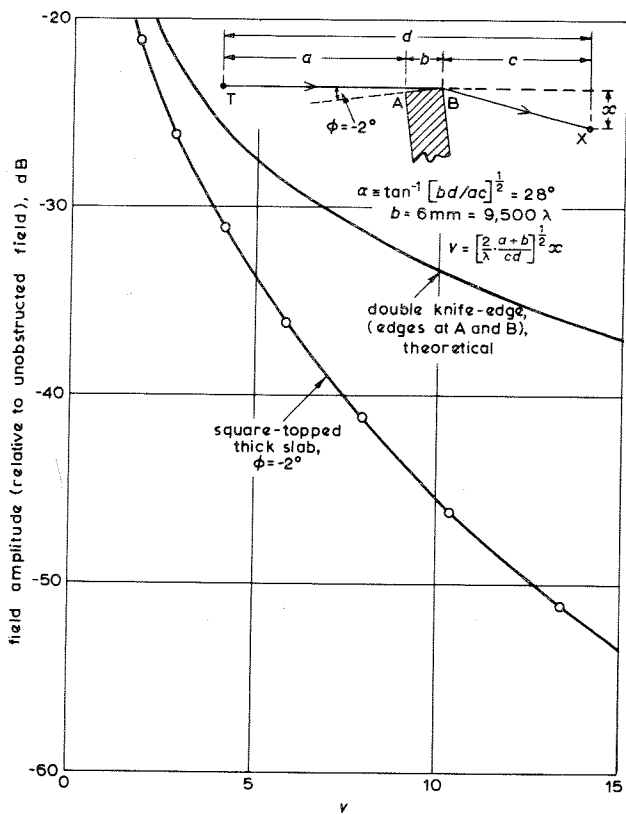
(c)

Fig. 29 - Shadow field variations for a square-top profile compared with that for a double knife-edge

$$\alpha = 28°$$

(a) $\phi = +2°$,   (b) $\phi = 0°$,   (c) $\phi = -2°$

6.3.2. The Square-Top Profile

This type of profile may be regarded as either a flat top, where the curvatures of the corners approach infinity, or a thick slab (see Section 3.5, Fig. 12, and the Appendix).

Detailed diffraction measurements were carried out on two square-top models with thicknesses of 6 mm (9500λ) and 1·25 mm (2000λ) respectively; in the configurations used for the measurements, the corresponding values of α were 28° and 13°.

The series of results displayed in Figs. 29(a), 29(b) and 29(c) is a comparison of the measured, relative field-strength variation in the shadow of the thicker (6 mm) model with the theoretical variation for a double knife-edge system of similar geometrical disposition (see inset diagrams). Each of the three Figures refers to a different inclination ϕ of the flat crest with respect to the transmitter horizon; the α-value of 28° was kept constant and the position of the receiver in the shadow is defined by the Fresnel parameter v, which refers to the equivalent (single) knife-edge.

Again, as with the flat-top models, it is clear that the flat crest of the obstacle has the effect of depressing the field strength in the shadow and that predictions based on a double knife-edge representation of the crest profile could seriously overestimate the field strength at positions well into the shadow.

The effect of the flat crest is considerably reduced if the surface is not smooth but randomly rough, and the broken-line curve in Fig. 29(b) illustrates this fact. The rough-surface result shown was obtained by repeating the diffraction measurement after covering the end-face of the model with a strip of the abrasive paper sample (c), whose statistical properties were given earlier (Section 5). It will be seen that the field variation is now closer to that of the double knife-edge system, as might be expected from the behaviour of rough-surfaced crests of constant (mean) curvature.

Fig. 30 illustrates the dependence of the field strength on the relative thickness (α-value) of a square-topped thick slab, for $\phi = 0$ (transmitter in the same plane as the flat crest). The plot points in this figure are measured values, while the continuous curves are the corresponding theoretical variations evaluated for this case using the method developed in Section 3.5. The agreement obtained here is encouraging and gives some experimental support to the theoretical method.

6.4. Polarization Experiments

Several measurements were duplicated for vertical as well as for horizontal polarization and the differences in shadow field strength were examined. Vertically-polarized radiation produced larger field strengths but the differences were found to be small, as expected from theoretical considerations. For example, Fig. 31 shows the ratio of field strengths for the two polarizations in the shadow of a smooth, rounded hill as a function of the excess-loss parameter r. The full-line curves are calculated, using the data given by Domb and Pryce, for two values of the modulus of the complex relative permittivity $|\epsilon_r| = 25$ and $|\epsilon_r| = 5$ respectively, assuming the hill has a radius of curvature of 16000λ. The circular plot points are the measured field-strength ratios for a polished aluminium cylinder also with a radius of 16000λ. No attempt was made to determine the optical constants of the particular commercial grade of aluminium used to construct the diffracting models. The complex refractive index of pure (bulk) aluminium, however, is known to be about 1·4–j5·2 at 589 nm, so that we would expect $|\epsilon_r|$ for the cylinders used to be somewhat less than $|(1·4–j5·2)^2|$, i.e. <29. Although Fig. 31 suggests that the effective value of $|\epsilon_r|$ for the model was substantially less than 25, the similarity of behaviour between metals at optical frequencies and ordinary terrain at v.h.f./u.h.f. is demonstrated.

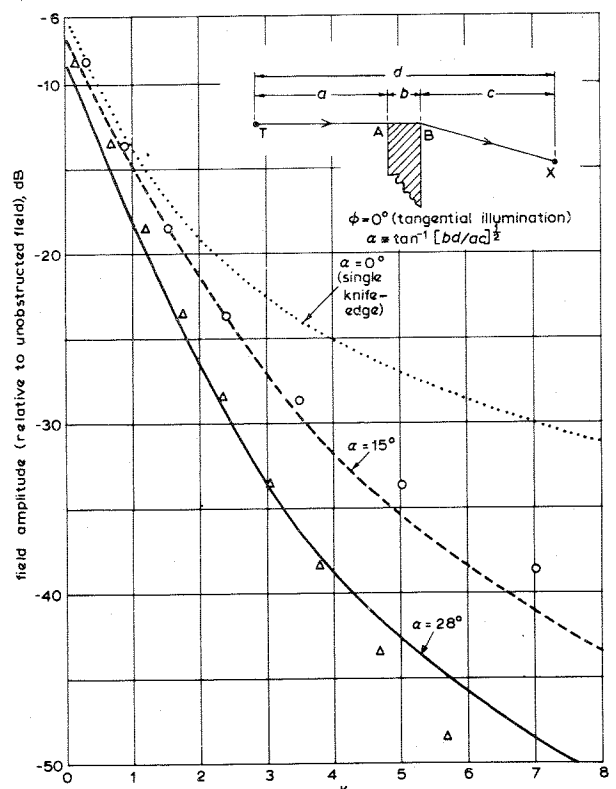Fig. 30 - Shadow field variations for square-topped thick slab: effect of slab thickness for $\phi = 0$

$\left.\begin{array}{c}\circ\\\triangle\end{array}\right\}$ measured values ------$\left.\begin{array}{c}\cdots\cdots\\\text{——}\end{array}\right\}$ theoretical curves
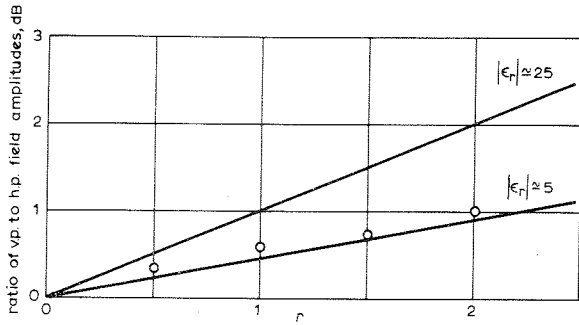
Fig. 31 - Shadow field-strength differences between v.p. and h.p. for a smooth hill of constant curvature, R = 16,000λ

o   Measured values for polished aluminium at optical frequencies

——   Calculated from rounded-hill theory at u.h.f.

The measured polarization differences, indicated in Fig. 31, were found to diminish to negligible values when the surface was made randomly rough. Thus it appears from both theory and laboratory measurement that the differences in shadow field strength between horizontally polarized and vertically polarized radiation at u.h.f. will be small and, for the great majority of rounded-hill profiles, no serious prediction errors are expected to arise if the orientation of the plane of polarization is neglected entirely.

7. CONCLUSIONS

The investigations outlined in this report confirm the following conclusions regarding propagation over rounded hills.

1. The field strength in the shadow is almost independent of the polarization of the incident radiation. Polarization differences diminish as the wavelength decreases and are negligible if the surface of the diffracting crest is randomly rough.

2. For predicting field strengths from ground profiles, the representation of a rounded hill by a single knife-edge, placed at the intersection of transmitter and receiver horizons, although usually good enough at v.h.f., may seriously overestimate the field strength at u.h.f.

3. Diffraction losses increase with increasing radius of curvature of the hill crest in the direction of propagation.

Further, the experiments yield the following new facts regarding the influence of the physical properties of a hill crest on its shadow field, with particular reference to u.h.f. propagation.

4. Random-type surface roughness always gives rise to an increase in the shadow field strength compared with the perfectly smooth surface, all other factors remaining equal. This appears to be true even if the curvature of the crest profile is not constant in the direction of propagation. Consequently, predictions which are based on smooth-body theories will always indicate the lower limit of the shadow field strength.

5. The dependence of the excess-loss (above that of a knife-edge) on a single parameter $\{r = (\pi R/\lambda)^{1/3}\theta\}$, which is a feature of far-field diffraction by crests of constant or slowly varying curvature, does not appear to be destroyed by making the surface randomly rough. It is therefore possible to take surface roughness into account by assigning an appropriate excess-loss function to the various types of terrain encountered in practice.

6. Flat-topped obstacles tend to cast very sharp shadows and the associated diffraction losses are high, especially if the flat portion is extensive and forms part of the actual crest profile. In the latter case, the field strength well into the shadow is approximately proportional to $b^{-1/2}$, where b is the length of the flat portion of the profile.

The following general approach is proposed as a basis for calculating shadow field strengths at u.h.f. from radial ground profiles. (It is assumed that these profiles are plotted on profile graph paper based on a 4/3 Earth radius to allow for normal atmospheric refraction.)

(a) Imagine a string stretched taut over the ground profile between the transmitting and receiving points. The string will then define a sequence of one or more tangents separated by curved arcs where it runs over any obstructing crests. Mark the intersection of consecutive straight portions and suppose the whole profile is reduced to a set of knife-edges situated at tnese tangent intersections. N.B.: Any hill-crests lying just below the imaginary string should be included.

(b) Calculate the diffraction loss (in decibels) for the system of knife-edges, using either the multiple diffraction method outlined in Section 3.4, or the Epstein-Peterson method[20]. The loss associated with two knife-edges is best calculated from the data given by Millington (Figs. 11 – 13 in Reference 13).

(c) Estimate the mean radius of curvature of each of the curved portions of the imaginary string and the associated angles of diffraction, from which calculate the magnitude of the excess-loss parameter r for each obstructing crest.

(d) If possible, make an assessment from a map

of the type of terrain in the region of each crest and, using the calculated r-values and appropriate excess-loss curves (Fig. 22), estimate the total curvature loss (in decibels) to be added to the knife-edge system loss. If the obstructing hill-crest is obviously a built-up residential area the excess-loss curve in Fig. 22 (sample (b)) is suggested as appropriate. (The present experiments indicate that appropriate excess-loss curves can be assigned to other types of terrain roughness, e.g. dense woodland, but further work is necessary to determine these specifically.)

(e) Further correction is advisable if the transmitter or receiver is very close to an obstructing crest. The theoretical correction outlined in Section 3.3 and shown in Fig. 10 is suggested, although no attempt was made to verify these data in the optical experiments.

(f) Although theory shows that the diffraction loss is less for vertical polarization the difference is not significant at u.h.f. unless the crest curvature is sharp and the terrain is smooth and well conducting. Should these conditions arise in practical work an approximate correction can be derived from Fig. 8.

The above procedure (a to f) is believed to afford a realistic estimate of the shadow losses when the obstructing crests are reasonably well isolated and their profiles are approximately circular arcs. Flat-topped hills and ridges are clearly exceptions and the general method may significantly underestimate the associated diffraction loss. For these varying-curvature profiles, it does not appear possible to present a simple method for predicting the excess-loss. However, the possible significance of the flat portion can be ascertained by calculating the α-value (see Fig. 12). If α is less than $15°$ the profile can be treated as a double-hump configuration without serious error. For larger α-values, a better approximation to a flat-topped crest is a thick slab for which the solution outlined in Section 3.5. is applicable, although the numerical calculation is rather complicated for the general case.

8. REFERENCES

1. CRYSDALE, J.H., DAY, J.W.B., COOK, W.S., PSUTKA, M.E. and ROBILLARD, P.E. 1956. An experimental investigation of the diffraction of electromagnetic waves by a dominating ridge. *I.R.E. Trans. Antennas Propag.*, 1957, AP-5, 2, pp. 203 – 210.

2. CRYSDALE, J.H. 1957. Comparison of some experimental terrain diffraction losses with predictions based on Rice's theory of diffraction by a parabolic cylinder. *I.R.E. Trans. Antennas Propag.*, 1958, AP-6, 3, pp. 293 – 295.

3. RICE. S.O. 1953. Diffraction of plane radio waves by a parabolic cylinder. *Bell Syst.tech. J.*, March 1954, Vol. 33, No. 2, pp. 417 – 504.

4. BACHYNSKI, M.P. 1963. Scale-model investigations of electromagnetic wave propagation over natural obstacles. *RCA Rev.*, 1963, XXIV, 1, pp. 105 – 144.

5. E.B.U. Technical Centre. 1966. The influence of the plane of polarization on the quality of television reception. *Tech. 3083-E*, March 1966.

6. PRYCE, M.H.L. 1953. The diffraction of radio waves by the curvature of the earth. *Adv.Phys.*, 1953, 2, 5, pp. 67 – 95.

7. WAIT, J.R. and CONDA, A.M. 1958. Pattern of an antenna on a curved lossy surface. *I.R.E. Trans. Antennas Propag.*, 1958, AP-6, 4, pp. 348 – 359.

8. FOCK, V.A. 1946. Diffraction of radio waves on the earth's surface. *Bull. Acad. Sci.*, USSR phys. ser., 1946, 10, 2, pp. 187 – 188.

9. WAIT, J.R. and CONDA, A.M. 1959, Diffraction of electromagnetic waves by smooth obstacles for grazing angles. *J.Res.Natn.Bur. stand.*, 1959, 63D, 2, pp. 181 – 197.

10. SHKAROFSKY, I.P., NEUGEBAUER, H.E.J. and BACKYNSKI, M.P. 1958. Effect of mountains with smooth crests on wave propagation, *I.R.E. Trans. Antennas Propag.*, 1958, AP-6, 4, pp. 341 – 348.

11. DOMB, C. and PRYCE, M.H.L. 1946. The calculation of field strengths over a spherical earth. *J. Instn elect.Engrs.*, 1947, 94III, 31, pp. 325 – 339.

12. RICE, P.L., LONGLEY, A.G., NORTON, K.A. and BARSIS, A.P. 1965. Transmission loss predictions for tropospheric communication circuits. N.B.S. Technical Note, 1965, 101, 1, pp. 7 – 4.

13. MILLINGTON, G., HEWITT, R. and IMMIRZI, F.S. 1961. Double knife-edge diffraction in field-strength predictions. *Proc.Instn elect. Engrs.*, 1962, 109C, No. 16, pp. 419 – 429.

14. MILLINGTON, G., HEWITT, R. and IMMIRZI, F.S. 1961. The Fresnel surface integral. *Proc. Instn elect.Engrs.*, 1962, 109C, 16, pp. 430 – 437.

15. FURUTSU, K. 1956. On the multiple diffraction of electromagnetic waves by spherical mountains. *J. Radio Res. Lab. Japan*, 1956, **3**, 14, pp. 331 – 337.

16. WILKERSON, R.E. 1966. Approximations to the double knife-edge attenuation coefficient. Radio Sci., 1966, **1**, 12, pp. 1439 – 1444.

17. Radio Research Laboratory, Ministry of Postal Services, Tokyo, Japan. 1957. Atlas of radio wave propagation curves for frequencies between 30 and 10,000 Mc/s. January 1957, pp. 172 – 9.

18. HACKING, K. 1966. Approximate methods for calculating multiple-diffraction losses. *Electron. Letters*, 1966, **2**, 5, pp. 179 – 180.

19. KELLER, J.B. 1962. Geometrical theory of diffraction. *J. opt. Soc. Am.*, 1962, **52**, No. 2, pp. 116 – 130.

20. EPSTEIN, J. and PETERSON, D.W. 1953. An experimental study of wave propagation at 850 Mc. *Proc. Inst. Radio Engrs.*, 1953, **41**, 5, pp. 595 – 611.

APPENDIX

Diffraction by a Thick Slab

Diffraction by two perfect knife-edges (strictly, two opaque, infinitely thin half-planes) in tandem has been treated by Millington et al[13], who applied Huygens' principle consecutively to the plane apertures above the edges, and manipulated the solution into a convenient form for numerical evaluation. This method yields the so-called classical solution of the diffraction problem which is sufficiently accurate for many practical situations where the distances involved are very much greater than the wavelength of the radiation.

The method can be extended to obtain the diffracted field behind a thick slab by supposing that it consists of two knife-edges which are joined by a plane surface as indicated in Fig. 32.
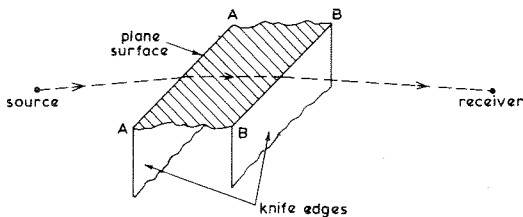

Fig. 32 - Thick-slab representation

The classical solution so obtained can be used to derive the diffracted field behind a thick slab of any specified surface conductivity and polarization of the incident wave.

The problem reduces to a two-dimensional one, and Fig. 33 defines the geometry of the cross sectional plane which contains the source T, the receiver R and the edges A and B (see Fig. 32).
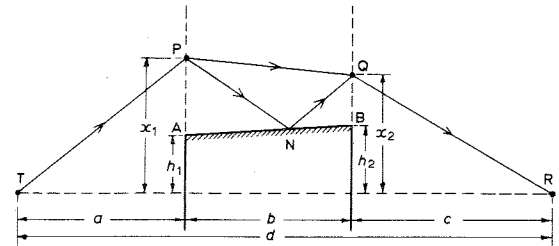

Fig. 33 - Geometry of thick-slab section

In Fig. 33, P and Q are arbitrary points, directly above the edges A and B, and distant x_1 and x_2 from the line TR respectively. Now radiation can be supposed to reach R via both of the two alternative paths TPQR and TPNQR. The former path is independent of the surface joining AB hence the component of the total field at R arising from path traversals of this type is that which would be obtained by two (unjoined) knife-edges situated at A and B respectively. Millington has shown that this field is proportional to the double integral

$$I = \int_{h_2}^{\infty} \int_{h_1}^{\infty} \exp\left\{\frac{j2\pi}{\lambda}\left[\frac{x_1^2}{2a} + \frac{(x_1 - x_2)^2}{2b} + \frac{x_2^2}{2c}\right]\right\} \, dx_1 \, dx_2$$

(13)

and, by the algebraic substitutions

$$u = \left[\frac{2(a + b)}{\lambda ab}\right]^{1/2}\left(x_1 - \frac{ax_2}{a + b}\right)$$

(14)

and

$$w = \left[\frac{2(a + b + c)}{\lambda(a + b)c}\right]^{1/2} x_2$$

(15)

he transformed Equation (13) to yield

$$I = \int_q^\infty \int_{f(w)}^\infty \exp\left[j\frac{\pi}{2}(u^2 + w^2)\right] du\ dw \qquad (16)$$

where $f(w) = p\ \mathrm{cosec}\alpha - w\ \cot\alpha$.

The parameters p, q and α are defined in terms of the distances a, b, c, d and the heights h_1 and h_2 (see Fig. 33) as follows:-

$$p = \left[\frac{2d}{\lambda a(b+c)}\right]^{1/2} h_1$$

$$q = \left[\frac{2d}{\lambda c(a+b)}\right]^{1/2} h_2 \qquad (17)$$

$$\alpha = \arctan\left[\frac{bd}{ac}\right]^{1/2}$$

From Equation (16), I is seen to be a Fresnel surface-integral and may be written

$$I = \int_S \exp(j\pi z^2/2)\ dS \qquad (18)$$

where the region of integration, S, is defined by the three parameters p, q and α, as shown in Fig. 34(a), and z is the distance of a point in the (u,w) plane from the origin $(u = 0, w = 0)$.

S is the sectorial region of the (u,w) plane extending to infinity and bounded by the straight lines $w = q$ and $w = p\sec\alpha - u\tan\alpha$.

Now consider the components of the field at R which arrive via paths of the type TPNQR which involve a reflection from the surface joining AB (Fig. 33). By similar reasoning using Huygens' principle we find their contribution to the total field at R to be proportional to $\rho I'$, where

$$I' = \int_{h_2}^\infty \int_{h_1}^\infty \exp\left\{\frac{j2\pi}{\lambda}\left[\frac{x_1^2}{2a} + \frac{(x_1-x_2)^2}{2b} + \frac{x_2^2}{2c} + \frac{2}{b}(x_1-h_1)(x_2-h_2)\right]\right\} dx_1\ dx_2 \qquad (19)$$

and ρ is the complex Fresnel reflection coefficient* of the surface AB. By making the substitutions

$$x_1 = X_1 + 2(ac/bd)\ [(1 + b/c)\ h_2 - h_1]$$
$$\text{and } x_2 = X_2 + 2(ac/bd)\ [(1 + b/a)\ h_1 - h_2]$$

Equation (5) can be transformed to

$$I' = \exp(j2\pi K)\int_{H_2}^\infty \int_{H_1}^\infty \exp\left\{j\frac{2\pi}{\lambda}\left[\frac{X_1^2}{2a} + \frac{(X_1+X_2)^2}{2b} + \frac{X_2^2}{2c}\right]\right\} dX_1\ dX_2 \qquad (20)$$

* The complex reflection coefficient is here assumed to be constant over the range of angles of incidence associated with the ray-paths through the first few Fresnel zones of the apertures above the edges.

where $H_1 = (1 + 2ac/bd)\ h_1 - 2(ac/bd)(1 + b/c)\ h_2$

and $H_2 = (1 + 2ac/bd)\ h_2 - 2(ac/bd)(1 + b/a)\ h_1$

The integral factor in the expression is now of similar form to that in Equation (13) and, as previously, can be converted into a Fresnel surface integral but with a different region of integration, S', as indicated in Fig. 34(b).
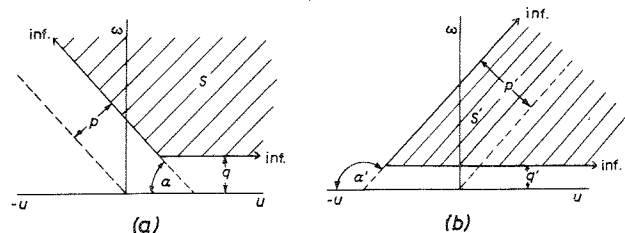

Fig. 34 - Regions of integration
(a) Direct component, region S
(b) Reflected component, region S'

The new region of integration is defined by the parameters p', q' and α' and it may be shown that these are related to p, q and α by

$$p' = \cot^2\alpha[(1 + \sec^2\alpha)p - 2q\ \sec\alpha]$$
$$q' = \cot^2\alpha[(1 + \sec^2\alpha)q - 2p\ \sec\alpha] \qquad (21)$$
$$\alpha' = \pi - \alpha$$

The exponential factor in the expression for I' (which signifies a constant phase shift) contains the constant K which, in terms of p, q and α, is given by

$$K = \cot^2\alpha[\sec\alpha(2\ \mathrm{cosec}^2\alpha - 1)pq - \mathrm{cosec}^2\alpha(p^2 + q^2)] \qquad (22)$$

The total field at R is the sum of the two component fields and is, therefore, proportional to $I + \rho I'$. In the absence of the diffracting obstacle the field would be proportional to the surface integral I taken over the whole (u,w) plane, which has the value 2j. Thus the total field E at R, relative to the free-space field, is

$$E = \frac{-j}{2}(I + \rho I')$$

i.e. $E = \frac{-j}{2}[I(p,q,\alpha) + \rho\ \exp(j2\pi K)I(p',q',\alpha')] \qquad (23)$